CHALMERS
UNIVERSITY OF TECHNOLOGY

Investigation of hot cracking in additive manufactured nickel-base superalloys

Process optimization and crack removal with hot isostatic pressing

Master's thesis in Material Engineering

EMIL HALLBERG

Department of Industrial and Materials Science
CHALMERS UNIVERSITY OF TECHNOLOGY
Gothenburg, Sweden 2018

MASTER'S THESIS 2018

Investigation of hot cracking in additive manufactured nickel-base superalloys

Process optimization and crack removal with hot isostatic pressing

EMIL HALLBERG

CHALMERS
UNIVERSITY OF TECHNOLOGY

Department of Industrial and Materials Science
CHALMERS UNIVERSITY OF TECHNOLOGY
Gothenburg, Sweden 2018

Investigation of hot cracking in additive manufactured nickel-base superalloys

Process optimization and crack removal with hot isostatic pressing

Emil Hallberg

Thesis was performed in the frame of the Centre for Additive Manufacturing – Metal (CAM^2) in collaboration with Quintus Technologies

Master Thesis 2018

Department of Industrial and Materials Science

Division of Materials and Manufacture

Chalmers University of Technology

SE-412 96 Gothenburg

Telephone +46 31 772 1000

Cover: Hot crack in a nickel-base superalloy manufactured by laser powder bed fusion

Gothenburg, Sweden 2018

Investigation of hot cracking in additive manufactured nickel-base superalloys
Process optimization and crack removal with hot isostatic pressing
EMIL HALLBERG
Department of Industrial and Materials Science
Chalmers University of Technology

Abstract

Additive manufacturing (AM) offers an unprecedented freedom of design and enables production of complex geometries with competitive mechanical properties, such as components for aerospace engines and gas turbines. Some commonly used materials, such as γ' precipitation strengthened Ni-base superalloys, are susceptible to cracking during both AM processing and subsequent densification and/or heat treatment. Therefore, to fully utilize the potential that AM offers, it is crucial to optimize the manufacturing process in order to minimize the amount of defects in the final product.

The aim of this study is to reduce the amount of defects, primarily micro-cracks, in a laser powder bed fusion (LPBF) processed γ' precipitation strengthened Ni-base superalloy. LPBF process parameter optimization, by using a design of experiment approach lead to reduction of defect density to very low levels. This was followed by a statistical data analysis to investigate how different parameters relate to defect formation. Furthermore, it is shown that post-AM hot isostatic pressing (HIP) can completely eliminate remaining micro-cracks. In addition, after HIP above a certain temperature and pressure (1210°C and 1000 bar), cracks did not re-open during subsequent high temperature heat treatment. SEM/EDX analysis showed that only small non-metallic inclusions remained after HIP+HT at these conditions. Finally, it is shown that by applying a tailored temperature-pressure profile, strain age cracking during HIP and heat treatment can be completely avoided.

Keywords: Hot isostatic pressing, Additive manufacturing, Laser powder bed fusion, Hot cracking, Nickel-base superalloys, strain age cracking

Acknowledgments

I would like to thank Quintus technologies for their expertise on hot isostatic pressing and that they offered to use their equipment for this project. I am also very thankful to my supervisor and mentor, Hans Gruber, who tirelessly helped and guided me in this project. Further thanks go to Lars Hammar who helped me with the AM machine and all the necessary software. Finally, I am grateful to my examiner and Chalmers together with everyone involved in making this project possible!

Contents

List of figures

List of tables

1
Introduction

In this chapter the reader will be introduced to the subject, aim and approach of this thesis. This introduction also aims to describe the problem, background and current state of additive manufacturing of similar materials.

1.1 Background and specific problem

Additive manufacturing with its unprecedented freedom of design potentially offers advantages over conventional subtractive manufacturing methods. However, due to the current state of additive manufacturing, the disadvantages outweigh the advantages most of the time and cheaper, more robust and reliable manufacturing methods are usually recommended. There are, however, some niche industries where the advantages make additive manufacturing a viable option, such as manufacturing of blades for aero engine and power turbines [1], which due to extreme heat during service are manufactured in nickel-base superalloys. When introducing a new alloy for AM production, its process window needs to be found and optimized, primarily with respect to the amount of defects, usually porosity, in the as-printed material. Furthermore, for additive manufacturing of nickel-base superalloys, one major obstacle is the appearance of so called hot cracks during printing. Hot cracking may have a detrimental effect on the performance of structural components, especially during cyclic loading [2]. It is a complex problem that can occur due to multiple metallurgical reactions together with the presence of residual stress. By controlling the process parameters, these effects can be mitigated, thus reducing the risk of hot cracking. Furthermore, as a complete defect elimination is unlikely with only process optimization, post-AM consolidation through HIP must be considered for critical parts [3], [4]. However, there is risk that defects that are seemingly eliminated during HIP may re-open during a subsequent heat treatment or in worst case even during service. In addition, these materials are susceptible to strain age cracking during post-AM heat treatment, which requires a careful control of the conditions also during this part of the manufacturing process.

1.2 Aim and formulation of problem

The aim of this thesis is to increase the knowledge regarding defects, especially hot cracks, in gamma prime (γ') strengthened nickel-base superalloys during laser powder bed fusion (LPBF) and how hot isostatic pressing can be employed for crack healing. Concerning the LPBF process, the main goal is to find the process window for production of defect free components. In addition, any effects of different process parameters on hot cracking will be investigated from statistical data analysis. Beyond LPBF parameter optimisation, a possible correlation between hot cracking and LPBF melt pool geometry is investigated. Furthermore, the possibility to use hot isostatic pressing (HIP) to enhance the material properties by reducing defects, with focus on hot cracks, is investigated. The crack healing effect is investigated by examining samples before and after hot isostatic pressing at different conditions. Furthermore, a correlation between HIP with subsequent heat treating and reopening of defect, if any, at elevated temperatures is sought. From this, this thesis work aims to address three main problems:

1. How LPBF process parameters relate to defect formation with focus on hot cracking.
2. If hot isostatic pressing can be used to close hot cracks and if they remain closed after a subsequent heat treatment.
3. How the temperature-pressure profile during post-AM HIP (and heat treatment) can be tailored to avoid strain age cracking.

The goal is that the results from this thesis will lead to optimal process parameters for LPBF and HIP with useful guidelines on the heat treatment for the investigated nickel-base superalloy.

1.3 Approach to the problem

Experiment matrices for the laser powder bed fusion, hot isostatic pressing and heat treatment processes are defined based on a literature review. All samples will be manufactured in-house by an EOS M290 laser powder bed fusion machine.

To find the optimal LPBF process parameters and to determine the robustness of the investigated material for the LPBF process, a wide range of samples will be investigated. The experiments are formulated using design of experiments (DoE) where all samples have a unique set of parameters. Presence of defects in samples produced with different process parameters are evaluated with light optical microscopy followed by image analysis. These data are analysed in a statistical analysis software to find any possible correlations between process parameters and defects, with focus on hot cracking. Melt pool geometries are examined by image analysis and correlated to process parameters and crack density.

Material densification with focus on healing of micro cracks through hot isostatic pressing (HIP) is evaluated from image analysis of metallographic samples examined before and after HIP. Since crack healing is affected by both temperature and pressure, several different HIP parameters will be evaluated. Possible re-opening of defects during heat treatment is examined from post-HIP samples that have experienced different thermal cycles. Scanning electron microscopy is employed to determine the nature of defects remaining after hot isostatic pressing and subsequent heat treatment and also to investigate the effect of HIP and HT on grain structure.

Strain age cracking during post-AM heat treatment is investigated from the occurrence of macro cracks in as-built samples after exposure to different temperature profiles.

2
Theoretical background

2.1 Material – Superalloys

Superalloys are a group of materials developed for elevated temperature service and are often exposed to an adverse set of high mechanical, thermal and chemical loads. Based on their major alloying element, they are divided into nickel-, cobalt-, iron-, and nickel-iron-base superalloys. Among these materials, nickel-base superalloys are often considered the most complex alloy system. They are designed for service at higher homologous temperatures than any other commercial alloy system and are extensively employed in the hot sections of aero engines and industrial gas turbines [1].

2.1.1 Nickel-base superalloys

Nickel-base superalloys have nickel as its main component together with several different minor alloying elements. A considerable amount of chromium is usually present which enhances the oxidation properties. Good oxidation and creep resistance with high temperature tensile strength makes them ideal for high temperature applications such as turbine blades. There are a variety of different nickel-based superalloys with varying chemical composition depending on the operational requirements. The most common alloying elements and their role are listed in Table 1. There are several strengthening mechanisms but the two most important ones are solid solution and precipitation strengthening [1]. One can divide nickel-base superalloys into weldable and non-weldable. Materials with high volume fractions of aluminium and titanium containing precipitation phases (γ’) are usually classified as non-weldable [1].

Table 1. The most common alloying elements in Nickel-based superalloys and their role. Total average in parentheses[5].

Element	Range in Nickel-base superalloys in wt.%	Role
Cr	1-28 (17)	Solid-solution strengthening, Carbide former and improves hot corrosion and oxidation properties.
Al, Ti	0-10 (3)	Solid-solution strengthening, γ' precipitation and improves oxidation properties.
Mo,W	0-28 (5.5)	Solid-solution strengthening, carbide former and increases γ' volume fraction.
Nb, Ta	0-6.5 (0.8)	Solid-Solution strengthening, carbide former and increase γ’ volume fraction.
Fe	0-38 (6)	Decreases oxidation resistance, used as filler to lower cost.
Co	0-29 (7)	Raises γ and γ' solvus temperature.
Ni	37-80 (57)	Main element, form FCC γ matrix phase and γ’.
C	0.01-0.4 (0.08)	Solid-solution and carbide former.
B, Zr	0-0.15 (0.02)	Solid-solution strengthening, improves grain boundary, creep and ductility.
Hf	0-0.35 (0.1)	Increase eutectic γ- γ' formation.

Boron, carbon and zirconium tend to segregate and form different phases at the grain boundaries. Nickel, cobalt, iron, chromium, molybdenum and tungsten prefer to form a face centred cubic crystallographic orientation (FCC) austenitic (γ) matrix. The Ni_3x elements, that is elements that form a compound with nickel, are aluminium, titanium, columbium (Niobium), tantalum and hafnium which contribute to precipitation strengthening. Usually strengthening mechanisms collaborate or gives strength at different temperatures which is one reason for the high amount alloying elements [1].

2.1.2 Phases in Nickel-base superalloys

Partly due to the number of elements in nickel-base superalloys there are several different phases that may form. A phase is defined as a portion of a system whose properties and composition is physically distinct from other parts of the system. Phase transformation is governed by Gibb´s free energy and if a system will have lower energy in another phase, a phase transformation will occur [6]. The energy in a system is affected by temperature and pressure, thus a change in temperature or pressure can lead to a phase transformation. Figure 1 shows different phases and how they change as a function of temperature in a nickel-base superalloy at constant pressure.

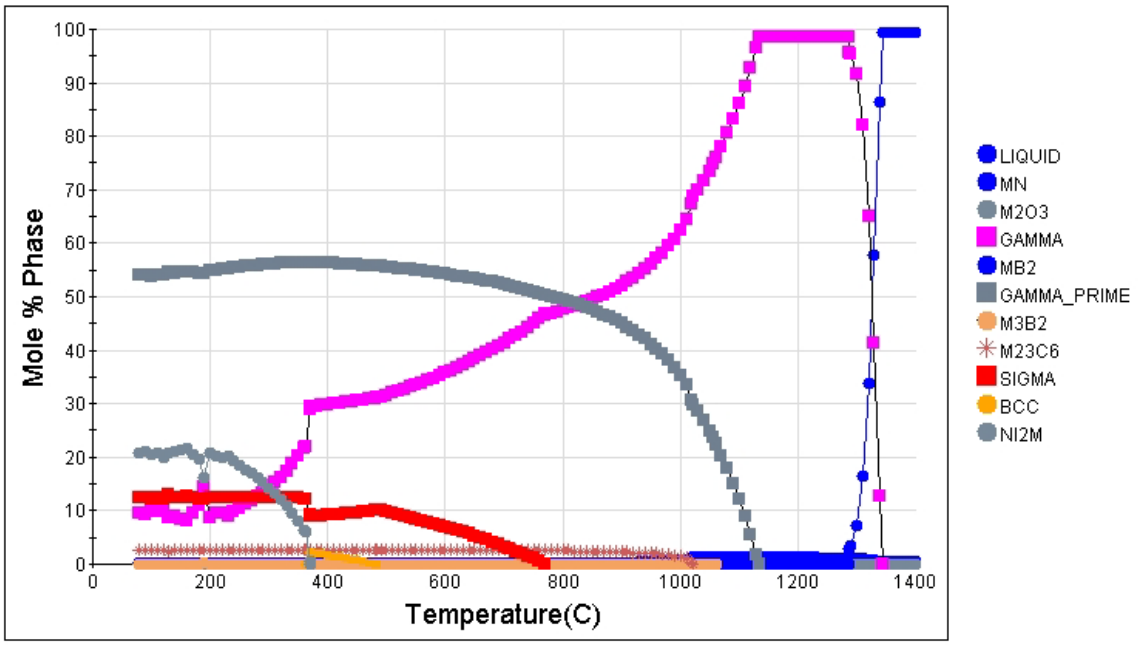

Figure 1. Phase diagram at a specific composition (from JmatPro).

The major phases present are listed below [1]:

1. The matrix phase, called Gamma matrix (γ) is an FCC austenitic phase with nickel as its main element.
2. The main precipitation strengthening phase, Gamma prime (γ'), gives super alloys its high temperature properties. γ' chemical composition is $Ni_3(Al,Ti)$ which makes aluminium and titanium γ' promoter. Alloying elements are added in proportion to precipitate high volume fractions of FCC γ'. A heat treatment is required to control and precipitate γ'.
3. Carbides is a group of phases formed by carbon together with another element that can form a non-intermetallic compound. Carbon combined with refractory elements such as titanium, tantalum and hafnium form MC carbides. At elevated temperatures, such as heat treatment or during service, MC carbides decompose to lower carbides such as M23C6 and M6C, which forms or segregates at the grain boundaries.

4. Borides such as MB_2 form at grain boundaries and hinder grain boundary tearing under creep rupture.
5. Topologically close packed, TCP, type phases can form in alloys if the composition is not optimal. These phases are unwanted and forms at elevated temperature during heat treatment service. Plate like phases such as σ, μ and laves form which lowers strength and ductility.

2.1.3 Strengthening of nickel-base superalloys

Nickel-base super alloys are strengthened by the same mechanism as many other metallic alloys such as solid-solution strengthening due to misfit in the matrix lattice and the solute atom, work hardening due to dislocation build up, grain boundary strengthening and precipitation strengthening. Precipitation is the main strengthening effect of nickel-base superalloys [1], [5] and is described more in detail below.

2.1.3.1 Precipitation strengthening

In precipitation strengthening, the FCC nickel matrix together with one or more of the γ' promoter form coherent particles, a phase called gamma prime (γ'), during ageing. Precipitation-strengthening works by hindering the movement of dislocations, which is the main mechanism of plasticity. When a particle, or precipitate, is present, dislocations must either move around or cut through the particles. Strengthening comes from the extra energy required for dislocations to alter their paths. A precipitate is formed when a super saturated material is aged. Super saturation is possible if a material has an increasing solubility with its alloying element at elevated temperature, as shown by the solubility slope in Figure 2. The solubility slope shows how much of a solute the parent material can contain at a certain temperature before another phase forms. If the parent material can have a higher amount of the solute at elevated temperature, it is possible to saturate the alloy.

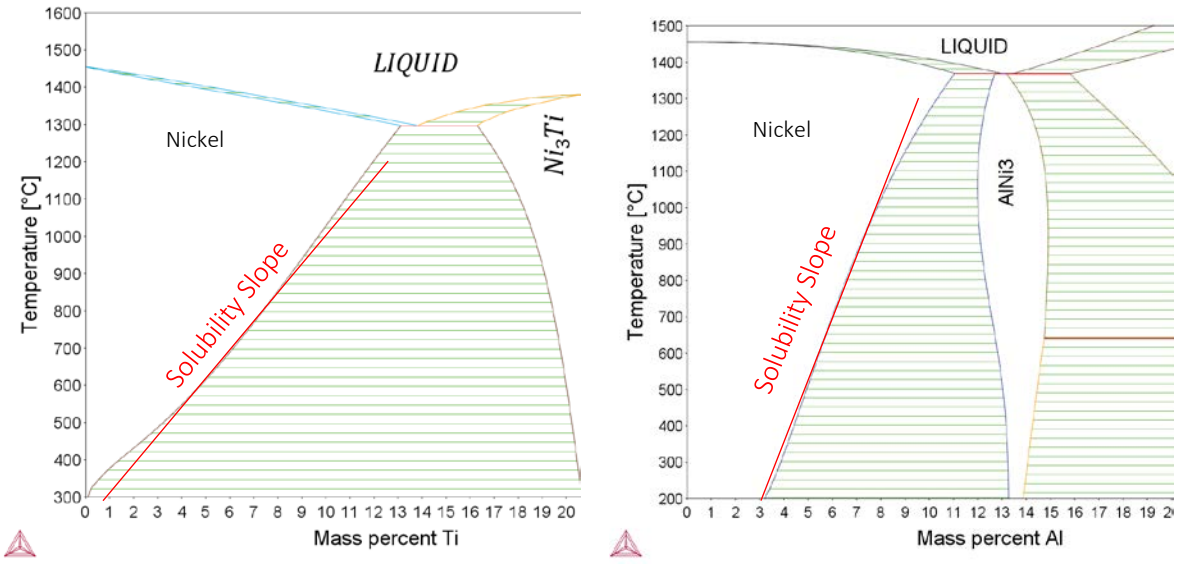

Figure 2. Solubility slope, Left: Titanium, Right: Aluminium in Nickel (from Thermocalc).

When holding at elevated temperature is followed by rapid cooling, or quenching, equilibrium is avoided and the precipitation forming element is locked in a metastable phase. By a subsequent heat treatment, or ageing, precipitates will form to lower the systems free energy. In nickel-base superalloys the strengthening precipitate, γ', is a coherent intermetallic compound. Due to coherency there will be a low mismatch between the matrix and precipitate which hinders the movement of dislocations. There are four main factors that controls the precipitates strengthening effect.

- The coherency strain that stems from lattice mismatch between the matrix phase and precipitates (γ / γ' mismatch). The coherency strain increases the energy required for dislocation movement.
- Antiphase boundary are high energy regions which requires extra energy per unit length for dislocation to pass.
- Volume fraction of gamma prime where high volume fraction is usually desired for high temperature applications.
- Size of precipitated particles ranges from a few nanometres to a few micrometres.

Volume fraction and size are the two factors controlled to tailor the precipitates and properties [7], [6], [1]. The amount and size of precipitates are tailored after service requirements.

2.2 Additive manufacturing and Laser powder bed fusion

In additive manufacturing (AM), also known as 3D-Printing, a physical component is built according to the geometry of a virtual model by adding material layer by layer, as compared to subtractive manufacturing where material is removed to form the desired geometry. This is done by slicing a virtual part into thin layers, shown in Figure 3, creating a stack of cross-sections. Each cross section is then manufactured by adding material layer wise and melting the cross-sectional pattern. This method enables creation of complex parts with similar mechanical properties compared to forging and casting [3].

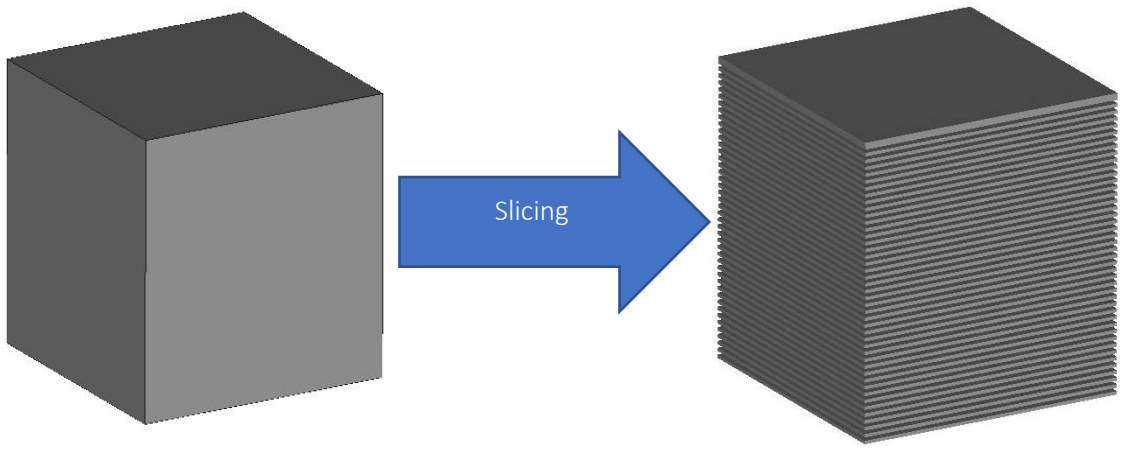

Figure 3: Representation of slices of a cube.

There are several types of AM methods that are designed for different materials and/or application areas. Powder bed fusion (PBF) is an additive manufacturing process where a thermal source fuses powder particle together to form the cross-section. In PBF a thin even layer of powder is spread, usually in the range of tens of microns thick, across the build plate. An energy source, either a laser- or electron-beam, then scans the cross-section and full melting takes place as the fusing mechanism. The whole bed is lowered one layer thickness and the new layer is filled with powder and the process is then repeated, as shown in Figure 4. The entire build volume is located in a sealed chamber with an inert gas such as argon. Laser powder bed fusion (LPBF) is a powder bed fusion based AM method which employs a laser as the energy source.

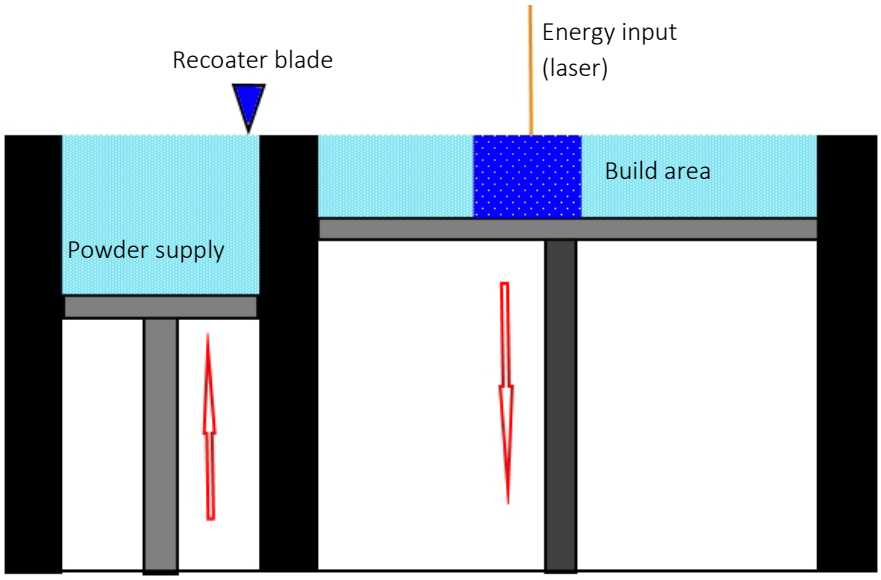

Figure 4. Selective laser melting with powder bed fusion

LPBF is one of the main AM method to use for engineering application and commercially manufacturing of components, especially low volume production series, with complex geometry or high demand on the microstructure [8]. Obtaining good quality in LPBF produced parts requires well-optimized process parameters. The main objective is to have sufficient energy to completely fuse the powder particles while remaining a good surface. However, other factors concerning the feedstock material such as thermal conductivity, solidus temperature and energy absorption must be considered as well to reach a stable and reproducible process. The microstructure of parts produced by LPBF is extremely fine and elongated in the build direction[9]. Buildability relates to the macro quality of the build. If a component has a rough surface it is still printable even if it is unsuitable for further use. If a component detaches from the build plate, hits the recoater blade or must be aborted, it is deemed unprintable.

2.2.1 Process parameters

The process parameters can be divided into four categories shown in Figure 5, which are dependent on and interacting with each other. Some of the major factors, or parameters, that affect the print quality, are listed in Figure 5. Pulse duration and frequency is only applicable for specific laser types and is not used here.

Laser Related	Scan related	Powder related	Temperature related
• Laser power • Spot size • Pulse duration • Pulse frequency	• Scan speed • Hatch distance • Scan pattern	• Particle shape • Particle size • Particle distrubtion	• Powder bed temperature • Powder feeder temperature

Figure 5. Some major factors affecting print quality

A simplified relation between the parameters is described by the volumetric energy density (VED). In its simplest form, it is laser power and scan speed related parameters that affects the energy input and gives the general equation, equation 1, for volumetric energy density [10].

$$E = \frac{P}{v*h*t} \quad [\text{J/mm}^3] \tag{1}$$

Where:

- *P* is laser power in Watt
- *v* is scan speed in mm/s
- *h* is hatch distance in mm
- *t* is the layer thickness in mm.

As an indirect measure of the energy input for fusing together the powder, VED also gives an indication of the size and shape of the melt pool. However, VED is simplified since it does not take other factors into account such as powder properties, heat of fusion, bed temperature etc. The reason for the simplification is that these four parameters are easy to change in the machine[11][3]. The general consensus is that these parameters and thus the VED influences defect density, such as cracks, lack of fusion and pores. Regarding cracking, Cloots et al [12] investigated crack and pore density as a function of scanning speed and hatch distance were the results point towards an increased crack density at higher VED while there is an increased pore density and bonding defect at lower VED. Table 2 list and effects of individual process parameters for LPBF.

Table 2. Parameter used in volumetric energy density

Laser power: The energy source for LPBF and heat input, measured in Watts. By varying the laser power, one directly affects volumetric energy density. Laser power is often related to defect density, too low power and the powder will not melt, too high power and the powder evaporates causing turbulence in the melt, resulting in a rough surface [10][3].
Scan Speed: The velocity of the vector from one point to another, measured in mm/s. By altering scan speed, the exposure time of the powder is changed and the VED can be controlled. Scan speed also affects the melt characteristics [3].
Hatch Distance: The distance between centrelines of two scan lines. Usually two scanlines overlap to minimize defects such as cracks and pores [13]
Layer Thickness: The thickness of each layer when slicing a part. Depends on machine precision and build quality and are included in the VED equation.

2.2.2 LPBF Microstructure

High cooling rates and small melt pools determines which phases are present and their morphology. Compared to conventional production methods, such as forging or casting, the microstructure in components manufactured by LPBF is much finer. Also, since AM utilizes 'layer by layer build up' there is always a preferred direction of solidification and cooling which makes it highly anisotropic. The heat will be transferred downward to previous built layers, support structure and into the build plate much faster than it will dissipate into the air. This results in an anisotropic microstructure with elongated grains in the build direction and small fine grains in the cross-sectional direction shown in Figure 6. Due to the fine microstructure in the xy-direction, the as-built material often has similar or higher strength than its casted or wrought counterpart[14].

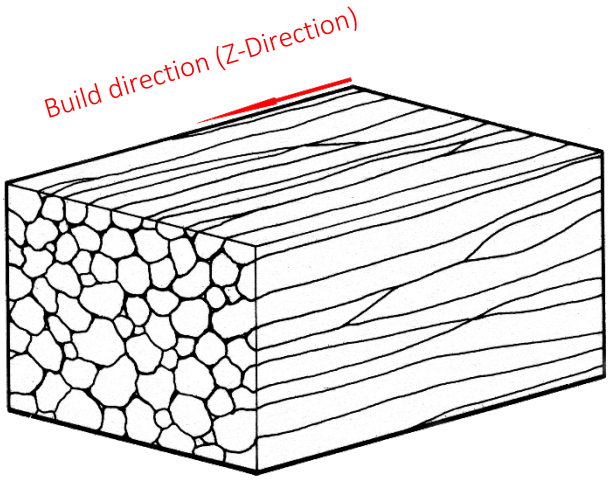

Figure 6. Schematics grain structure of additivly manufactured parts

2.2.3 Melt pools in LPBF

Due to the nature of LPBF, as with welding, where material only melt locally at the energy source surrounded by the heat affected zone (HAZ) there will be a characteristic shape of the solidified structure. In welds there is often only one or few weld bead but with higher energy input and thus a larger HAZ compared with LPBF where the HAZ is small but scanned across the entire cross-section and is stacked in layers, efficiently built by several weld beads [15], [16]. The size of the isotherm for welding and LPBF varies in size which is represented in Figure 7.

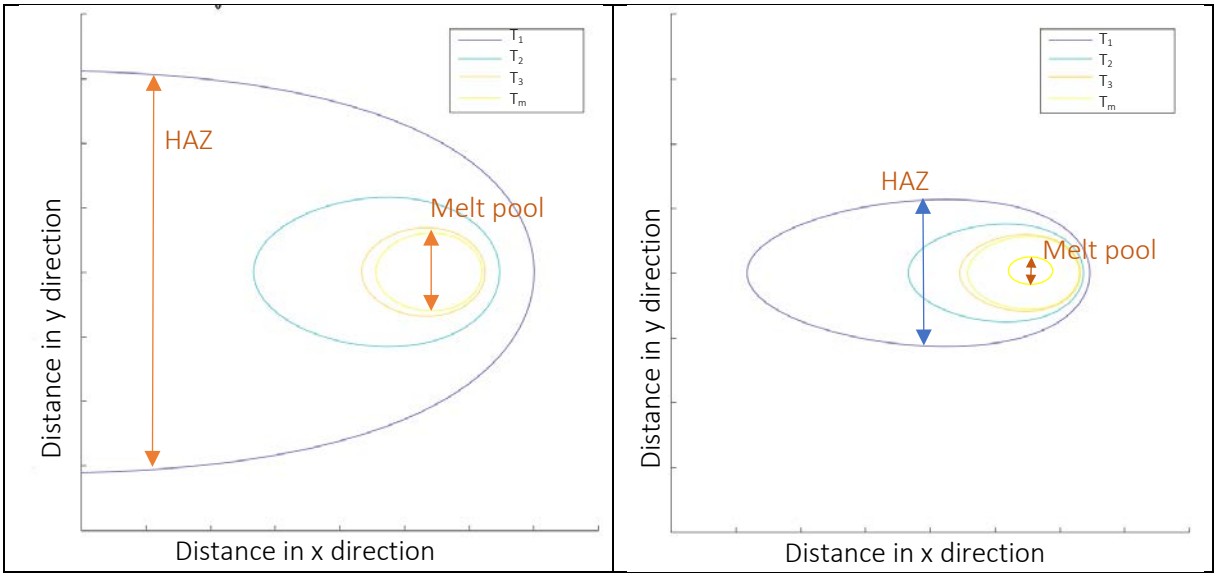

Figure 7. Schematic comparison of HAZ for seen from above. Left: Welding, Right: LPBF

The shape and size of the melt pool is related to both liquation and solidification cracking in welding. A larger melt pool has a longer solidification time which increases the risk of constitutional liquation in the HAZ while a smaller melt pool experience less segregation. Due to the similarities to LPBF it could affect cracking in LPBF manufactured parts as well [17][12]. Regarding weld pools, it is the depth-to-width ratio and geometry that affects cracking in welds. With a high depth-to-width ratio, e.g. with a deep melt pool, there is an effect called keyholing. Keyholing appears when the melt pool penetrates a deeper and smaller section in the material. This smaller section will experience higher residual stresses from the solidification of the material, shown in Figure 8. Cloots et al [12] found three distinct shapes of the melt pool that is correlated to different scanning speed with constant power, i.e. volumetric energy density. At the highest energy density there were frequent keyholing while at intermediate energy densities the general shape was a 'half ellipse' and at the lowest energy density the melt pool had 'bead'

shapes. Figure 8 illustrates the influence of scanning speed on the penetration depth and melt pool shape. In Figure 8 the melt pool is seen as a cross-section and not along the scanned path and show how depth influence the melt pool shape. Higher residual stress is formed by the melt pool where a deeper penetration takes place, indicated by the high angle. When the penetration is less deep the residual stresses are more evenly spread, as indicated by the lower angle.

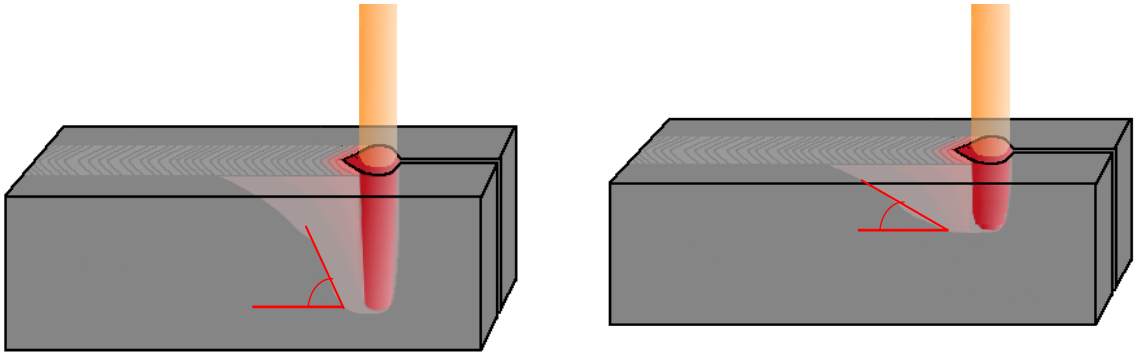

Figure 8. Melt pool depth formation. Left: Lower scan speed and higher residual stress in the keyhole. Right: Higher scan speed and lower residual stress with no keyholing. Adapted from [31]

2.2.4 Defects in LPBF

Typical defects found in LPBF components are microcracks, lack of fusion, pores and unwanted phases, such as oxides. Common for all defects is a reduction in performance by lowering mechanical properties of the material. Lack of fusion is highly influenced by the energy input and can be controlled by optimization of processing parameters. Although cracks and pores are influenced by the parameters they are hard to remove completely. Oxides are minimized by using an inert atmosphere during printing and heat treatment. There is also a risk of failed print if the surface of printed parts is too rough which is caused by a too high energy input [11].

2.2.4.1 Cracks

Cracking occurs when strain exceeds the materials ability to deform. In bulk material where no external stress is applied, the thermal induced strain may locally be much higher than the average global strain and thus small cracks may occur separately, not prompting a fracture. When there is a liquid phase present, the material experience zero ductility around the liquid film, which increases the risk of crack formation. Precipitation strengthened materials, often classed as non-weldable, can crack during heat treatment because there is a dip in ductility and a spike in hardness when a certain volume percent of precipitates is reached. If there is strain present, as in the case of LPBF produced parts where the thermal cycles create residual stresses, combined with volume expansion due to heating, there is high risk of cracking [1]. Three major cracking mechanism that are relevant and explained more in detail below.

2.2.4.2 Solidification cracking

Solidification cracks are often intergranular and have a dendritic structure due to the difference in solute concentration during solidification. During solidification, solute segregates towards the liquid phase which lowers the eutectic temperature and the liquid becomes constitutionally undercooled [6]. This suggest that solidification cracking occurs in the final stages of solidification where dendrites are almost fully grown into grains that are separated by a thin liquid film at the grain boundaries [17]. A liquid film weakens the grain boundary and due to the nature of additive manufacturing, which has a high geometrical constraint, there is stress acting on the boundaries due to thermal contraction. Figure 9 shows how a typical solidifaction crack is oriented where the last liquid solidified in a melt pool.

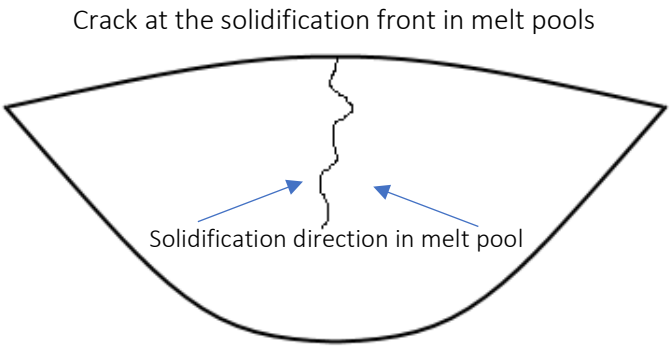

Figure 9. Typical Solidification cracking in a melt pool at the solidification front.

For solidification cracking in welds, there are several factors that needs to be considered [17].

- The solidification temperature range, which changes if there is stirring/mixing or sufficient time for diffusion during solidification. The solidification range is also highly affected by the alloy chemistry as some alloying elements tend to form low melting phases through segregation during solidification.
- Amount and distribution of liquid in the last stage of solidification, the last liquid to solidify will have a higher concentration of solute then the rest of the material and might show brittle behaviour.
- Surface tension of the grain boundary liquid. Surface tension is related to the wetting of the melt, adhesion of liquid to solid and thus the ability to from a continues film on grains.
- Geometric constraint is a factor that cannot easily be changed in additive manufacturing but according to Gibson et al [3] it is possible to mitigate this factor by controlling scan pattern.

Weld metal tends to shrink due to thermal contraction and this plays an important part in cracking [3]. In welds this mechanism may form macro cracks but since the thermal source and heat affected zone is smaller in LPBF, microcracks can also form.

Melt pool depth-to-width ratio is an interesting approach to reduce solidification cracking and is applicable to AM. When a melt pool solidifies, due to contraction, residual stresses can form at the melt pool boundaries. A deeper and narrow melt pool will experience higher residual stress which is why guidelines for melt pool formation has been developed [18].

2.2.4.3 Liquation cracking

Liquation cracking, just as solidification cracking, is intergranular but there is no dendritic structure on the cracked surface. In welding, liquation cracks appear inside the partially melted zone, located directly outside the fusion zone, as compared with solidification cracks that occur in the fusion zone. Liquation can appear both in the grain boundary and within the grains. It is grain boundary liquation that give rise to liquation cracking. As mentioned above, a liquid phase in the grain boundary weakens the material and cracks can appear if there is sufficient residual stress. With an increasing amount of a liquid phase, there is an increasing risk of liquation cracking. Liquation cracking is more prevalent in materials with large grains. Since additive manufacturing produce small elongated grains, as shown in Figure 6, there should be higher risk of liquation cracking in the build direction [17]. The main mechanism for liquation cracking relies on the fact that in the partially melted zone phases with different melting temperature exists. These phases melts while the surrounding material remains solid, causing liquation cracks.

2.2.4.4 Strain age cracking

Strain age cracking (SAC) is caused by loss in ductility when ageing a strained material. Strain usually comes from the thermal contraction and expansion during welding or AM processing. SAC occurs in a critical temperature interval, depending on alloy composition. During aging when precipitates form and if the phase transformation is faster than the materials relaxation response, cracks may occur. For γ' strengthened materials, such as some common nickel-base superalloys, the precipitation of γ' is rapid at elevated temperature, as shown in Figure 10. The rapid precipitation of γ' leads to a peak in hardness and consequently a rapid drop in ductility. The rapid drop in ductility means that previous acceptable levels of strain is higher than the new limit of the material and thus cracks can form.

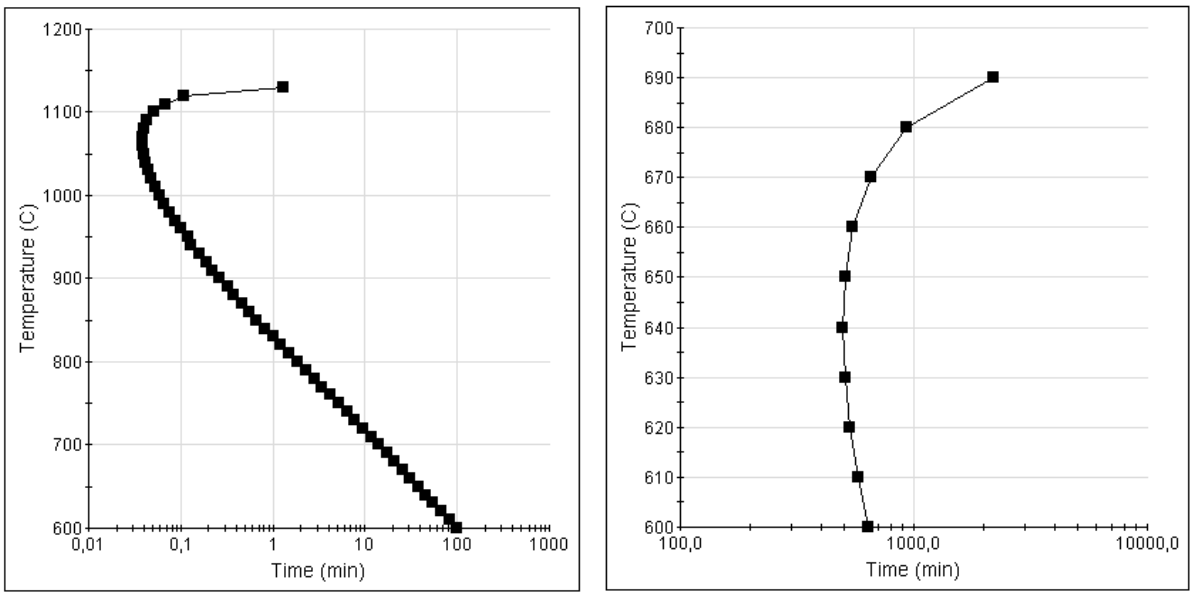

Figure 10. TTT diagram of a Nickel-base super alloy. Left: γ' precipitation is rapid. Right: γ'' precipitation is slow

As shown in Figure 10 above, by tailoring the chemical composition it is possible to create a material that is more resistant to SAC. Figure 10 (left) shows a nickel-base superalloy that form $Ni_3(Al,Ti)$ (γ'); at 1000°C the formation starts after a few second. Compared to the right figure which shows a much more sluggish formation of Ni_3Nb, called γ'', that takes hours to form [1], [7].

2.3 Heat Treatment

Heat treating in general can be divided into stress relieving, annealing and solution treating plus quenching followed by ageing. Each of which is done at different temperatures, holding times and sought properties.

Stress relieving is not always a necessary step to perform and its only purpose is to remove residual stresses. LPBF components possess a substantial amount of residual stresses due to the high thermal gradients combined with geometrical constraints. To stress relief an age hardenable alloy can be difficult since often the required temperature for stress relieving is enough to form precipitates, and often falls in the upper temperature range for aging. Stress reliving temperatures are below annealing and recrystallization temperatures. Figure 11 show a typical stress reliving curve and the drop-in ductility that occurs in gamma prime strengthened materials. It is quite fast to remove the peak residual stress while it takes longer time to get rid of all the residual stresses. However, only a small percentage of the stress is relived before the ductility drops below a critical level and SAC occurs as mentioned in section 2.2.4.4. The actual temperature used varies greatly depending on material [19].

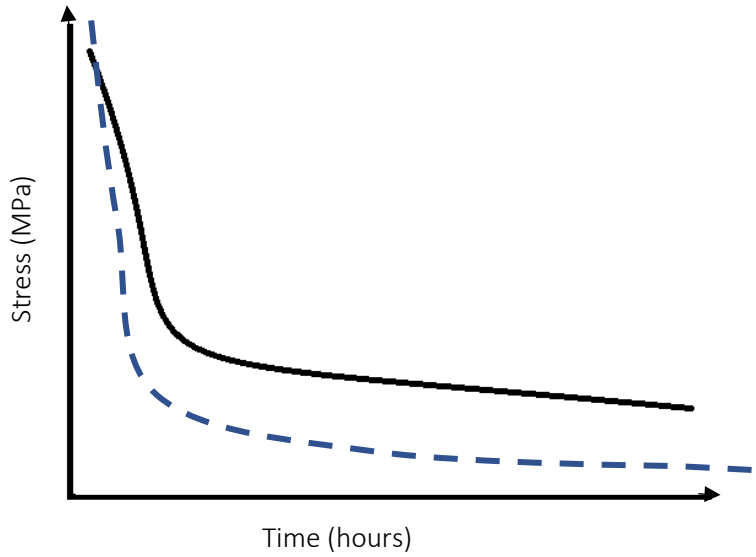

Figure 11. Solid line shows a typical stress reliving curve. Dotted line illustrated the drop-in ductility

Annealing, or full annealing as it is called, involves complete recrystallization and results in maximum softness. Annealing is used to reduce hardness and increase the ductility to improve formability and machinability [19].

Solution treating and *quenching* is usually the first step in the precipitation hardening of superalloys. The main objective for solution treating metals is to dissolve all unwanted phases so a well-controlled ageing can take place. Solution treating is performed between γ' solvus and melting temperature in the heat treatment cycle. After a solution treatment the material is quenched, or rapidly cooled, with the purpose to maintain the supersaturated solid solution obtained during solution treatment. For alloys sensitive to strain age cracking a high heating rate is required [19].

Ageing is performed on the super saturated solid solutionized material. By ageing the material it is possible to control the grain size and principal aging phase. By holding the super saturated material at elevated temperatures, precipitates starts to from and grow. The size and volume fraction is controlled by holding time and temperature. The desired size depends on service conditions [19], [6].

2.4 Hot isostatic pressing

Hot Isostatic pressing (HIP) is widely used for removal of pores or to fully densify green powder parts. Even if the HIP process was developed for diffusion bonding and pore removal of ceramics, the major activity has shifted to the consolidation of metal powder and densification of castings. HIP is a combination of sintering, which occurs when heat is applied to powder or a component containing pores, and cold isostatic pressing which uses high pressure to densify powder. HIP works at elevated pressure, up to a couple of thousand bars, and at high temperatures to fully densify a part. The isostatic pressure in HIP stems from molecules or atoms of gas that are colliding with the surface of an object. The gas atoms are moving extremely fast which generate up to 10^{30} collisions every second per square meter. Every surface of the HIPed object is experiencing the collisions and the pressure acts in a direction normal to the surface on all surfaces. The hipping conditions, temperature and pressure, are chosen so that the pressure is above the reduced yield stress at the elevated temperature. This allows plastic flow and creep to collapse and close the pores. The pressure required for densification, or closure of pores, depends on the size and content of pores but a pore with a diameter of 0.1 mm will require a pressure of 0,4 bar [4]. This is low compared to the pressure usually applied which is around 1000-2000 bar. The temperature to reduce the yield stress is usually above $0.7*T_m$ which also

is enough to allow for creep and diffusion. For nickel base superalloys the HIP temperature should be above the γ' solvus temperature to allow for creep [20]. Since the pore is not only closed by shear force, which would create a planar crack, but bonding also occurs because atoms diffuse in both direction across the newly formed interface, effectively closing the crack [4]. However, gases are soluble to different degrees and some gases cannot be dissolved in the matrix, pores containing argon may not close. If a component is heated without pressure, swelling may occur which can enlarge the pores or even cause cracking. Thus, it is important to minimize gas in pores by controlling the manufacturing process before HIP. Tammas-Williams et al [21],[22] among other show that there is a possibility that successfully closed defect during hot isostatic pressing have a risk of opening again during subsequent heat treatment. It is theorized that the reason for this is that the gas used in hipping or trapped during LPBF is non-soluble with the hipped material. For example, argon is non-soluble in metals and there is a risk during post HIP heat treatment that trapped gas exerts enough pressure to reopen some of the cracks and pores.

As a result from the elevated temperature and applied pressure there is also a change in microstructure and grain size. This will also lead to a change in mechanical properties and may reduce the scatter in strength which is important for both fatigue and creep life. However, some fine oxides are typically still left in the material after hipping due to their high thermodynamic stability and low oxygen solubility in the matrix. Furthermore, hipping can only close non-surface pores and cracks. If a pore is connected to the surface, and thus open to the hipping gas, it will act as an independent surface and no densification is possible [4]. Zhaop et al. [13] showed that full micro-crack healing is plausible in the material René88-DT. However, larger cracks in the range of 3-10 mm had a high risk of MC carbides nucleation even though they did fully close.

2.5 Design of experiment

For engineers and scientists, experiments are generally performed to create, test and confirm a hypothesis regarding a process. Design of experiment, or DoE, describes how an experiment should be performed to correlate input and factors, with output and the response, while maintaining a high statistically accuracy and good reproducibility. The factors are independent of each other but can trigger similar responses, and the design should be such that it is possible to determine which factor affected the output. Uncontrollable factors, external factors or other interference are termed noise and should be kept the same or similar in all experiments [23], [24]. Figure 12 show graphically how input, noise and controlled factors are often entangled and often there is not always a clear correlation.

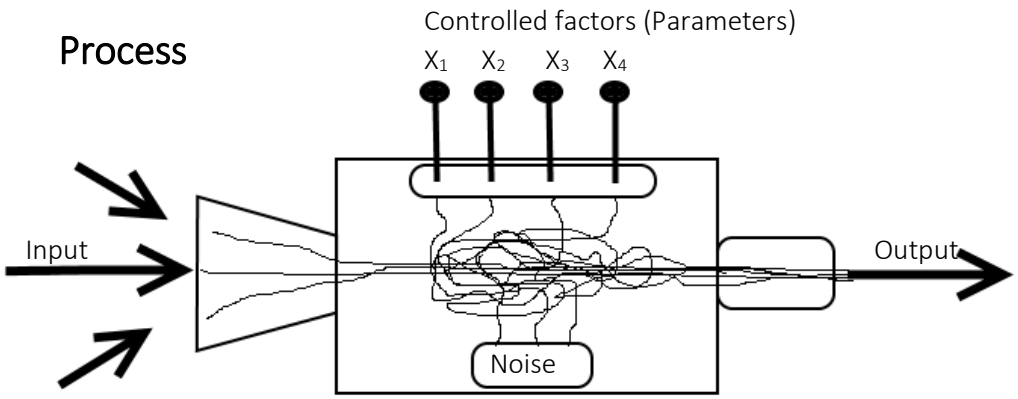

Figure 12. Illustration of an experiment and how the different inputs tangles together.

The controlled factors in this experiment are the parameters, Laser power (X_1), scanning speed (X_2) and hatch distance (X_3). It is important to choose a model that fit the experiment which simplifies and enables a statistically sound data analysis with easy to measure input and factors [24].

When using design of experiment the selected factors, input and responses are formulated into a matrix, which can graphically be visualized. Two examples are shown in Figure 13. A design of experiment usually consists of different runs and after each run the next design matrix adapts do the results from the first design to get as much data as possible.

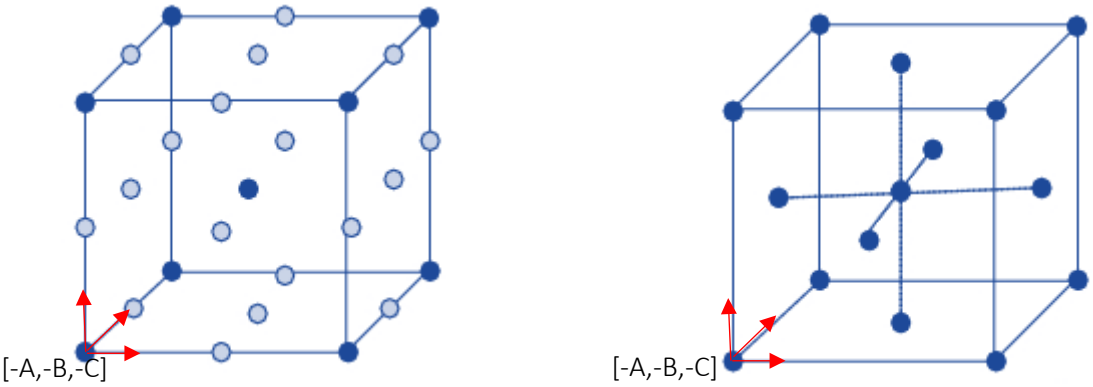

Figure 13. Data points that forms a geometry in a 3D space. Left; A full factorial design. Right: A fraction factorial design

2.5.1 Factorial experiment design

One of the most commonly used design of experiments is a full factorial design and is useful for smaller experiments where the design parameters are less than or equal to four. A full factorial design consists of all possible factor combinations, or variables, and factor levels, or values. From a factorial design all possible results that can be derived from factors and their levels are studied [23], [25].

From a statistical point of view, when factors have values an equation can be used to correlate factors with the response.

$$Y_{ijk} = u + \alpha_i + \beta_j + (\alpha\beta)_{ij} + \cdots + \varepsilon_{ijk} \quad (1)$$

Where i and j are levels of factor α and β, respectively, and k is the number of experimental units in the ij parameters. (αβ) is the effect of interaction between α and β for the different levels, u is common mean of all treatments and ε is the experimental error. In a full factorial design, the number of experiments required is given by the number of levels to the power of number of factors, which is n^k. For example a 2-level design with 3 factors require $2^3 = 8$ combinations [23][25].

2.5.2 Fractional factorial design

By carefully choosing factors of a factorial experiment design it is possible to reduce the number of experiments required. The values for the factors are chosen to fulfil the 'sparsity of effects' principle, which states that a system usually is dominated by main effect and secondary interactions. By obeying this principle, it is possible to investigate the most important features of the experiment while using 'fraction' of a full factorial experiment. The number of experiments required is defined as $n^{(k-p)}$ where as in a full factorial, n is the number of levels, k is the number of factors and 0.5^p is the fraction of the full factorial n^k. For example, $2^{(5-2)}$ is a quarter of a fraction of a 2-level design with 5 factors[23]. That is, there is a reduction in required experiments from 32 to 8, shown in Figure 14 and the design matrix is shown in Table 3.

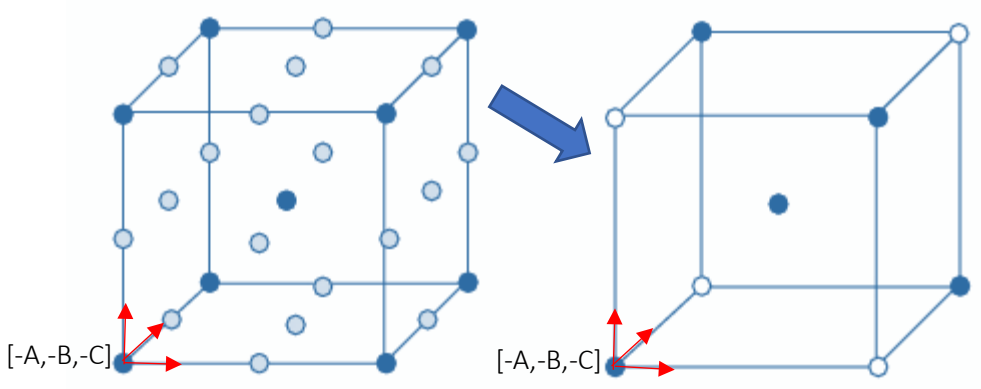

Figure 14. Conversion of a full factorial design to a reduced fractional factorial design.

Table 3. Design matrix with the fractional factorial points

Run / sample	A	B	AB	C	AC	BC	ABC
1	-1	-1	1	-1	1	1	-1
2	1	-1	-1	-1	-1	1	1
3	-1	1	-1	-1	1	-1	1
4	1	1	1	-1	-1	-1	-1
5	-1	-1	1	1	-1	-1	1
6	1	-1	-1	1	1	-1	-1
7	-1	1	-1	1	-1	1	-1
8	1	1	1	1	1	1	1

There are many different types of factorial designs which are all suitable for different scenarios. In Figure 14, the design matrix creates a square when presented graphically, the numbers in the matrix represent a coordinate, but there are other types which creates different figures. If one does not need the extreme points, they can be replaced and thus creating a different graphically representation. Two commonly used matrix designs are Taguchi´s and Doehlert methods. Taguchi is a fractional factorial that requires less data points but more measurements while Doehlert uses more data points but avoids the extreme points.

2.4.3 Response surface methodology

Response surface methodology (RSM) is used to visualize data graphically. By creating and connecting data points, a line or surface can be constructed visually presenting data. RMS is built around mathematical and statistical techniques to be able to visually create and interpret the data. The response, y, and a number of inputs, $x_1,x_2,x_3....x_n$ is used and even if the relationship is unknown it can be approximated by a low-degree polynomial model of the form

$$y = f'(x)\beta + \epsilon \quad (2)$$

Where x = ($x_1,x_2,x_3....x_n$) and f(x) is a vector function of p elements with varying relations, such as to the power of … , to $x_1,x_2,x_3....x_n$, up to a certain degree. B is a vector of p unknown constants coefficients called parameters while ε is a random experimental error with zero mean. There are two models that are commonly used in the response surface methodology approach and are a development from model 1 which includes a first-degree model

$$y = \beta_0 + \sum_{i=1}^{k} \beta_i X_i + \epsilon \tag{2}$$

And a second-degree model

$$y = \beta_0 + \sum_{i=1}^{k} \beta_i X_i + \sum_{i<j}^{k} \beta_{ij} X_i X_j + \sum_{i=1}^{k} \beta_{ii} X_i^2 + \epsilon \tag{3}$$

Figure 15 below shows different polynomial degree and a curve fitted for obtained data points.

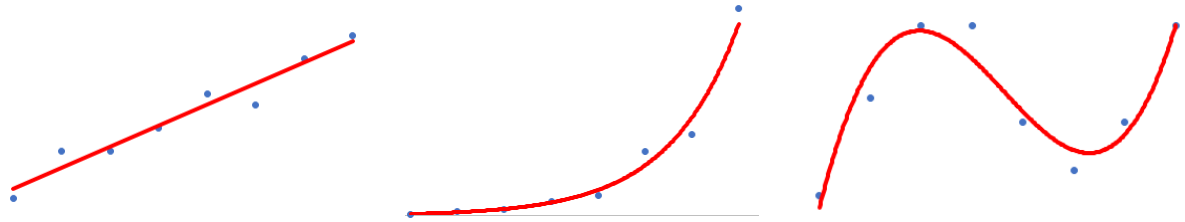

Figure 15.Left: Linear-response. Middle: Second-order response. Right: Third-order response

The goal is to find an approximate relationship between the output, y, and the input, $x_1,x_2,\ldots,x_n$, so a prediction model can be formulated. By formulating experiments and testing the significance of factors the experiment is evaluated and validated. After which the optimum settings of the inputs can be determined [26].

To evaluate the response, one must first obtain the coefficients β for the polynomials which can be found by conducting for a series of *n* experimental runs. In each of these experimental runs the response is measured and expressed in a so-called *response surface design matrix*. The design matrix, *D* in the order of *n x k* is expressed:

$$D = \begin{bmatrix} x_{11} & x_{12} & \cdots & x_{1k} \\ x_{21} & x_{22} & \cdots & x_{2k} \\ \vdots & \vdots & \ddots & \vdots \\ x_{n1} & x_{n2} & \cdots & x_{nk} \end{bmatrix} \tag{4}$$

Each point in the D matrix represent a design point, or a sample, which together maps a geometry in a k-dimensional space. Each run will create a response, e.g. y_5 is the response of the fifth run with $X_5=X_{51},X_{52},\ldots X_{5k}$. By creating a new model matrix, X with *n x p* number of elements one for each response expressed as

$$y = X\beta + \epsilon \tag{5}$$

The matrix, X, contains one column for each coefficient, β_n, and the intercept. Assuming ε has a zero mean the coefficient vector, β, can be predicted from the so-called *least-square formula*.

$$\beta = (X'X)^{-1}(X)_y \tag{6}$$

One advantage of the response surface matrix is the ability to fit first-, second- and third-degree polynomials over different regions in space. Usually one start with a first degree polynomial and if the response show a higher level of curvature a second or even third degree is required to accurately predict the response[26][25].

3
Experimental Methods

There are three main goals in this project. The first goal is to find optimal LPBF parameters for the current material and to correlate each parameter, or combination of parameters, to defect density with a focus on micro-cracks. The second goal is to evaluate how hot isostatic pressing affects crack density by investigating if and when crack healing occurs. The third goal is to investigate if crack opening occurs when a post HIP heat treatment is applied and how the grain structure is affected by hot isostatic pressing.

3.1 Nickel-base superalloy

The material used for this project is a γ' strengthened nickel-base superalloy variant with a combined aluminium and titanium content of roughly 7 wt. %. The powder is gas atomized with size of 25-63 µm and was provided by Höganäs AB.

3.2 Laser powder bed fusion machine – EOS M290

The LPBF machine used to produce samples for this project is an EOS M290 which is employed by the industry to manufacture components with high quality and good reproducibility[27]. The relevant technical specification is shown in Table 4.

Table 4. Technical specification of EOS M 290. From https://www.eos.info/eos-m290

EOS M 290	
Building volume	250 mm x 250 mm x 325 mm (9.85 x 9.85 x 12.8 in)
Laser type	Yb-fiber laser; 400 W
Precision optics	F-theta-lens; high-speed scanner
Scan speed	up to 7.0 m/s (23 ft./sec)
Focus diameter	100 µm (0.004 in)
Power consumption/supply	max. 8.5 kW (typical 3.2 kW) / 32 A

3.3 Optimal processing parameters

There are different approaches to data collection and this project follows the 'experimental approach' where data collection is performed based on experiments. To make it easier to analyse, data is usually organized in two dimensions. One dimension represents the input and can be a combination of one or several parameters while the second dimension is the output or in this project, crack density.

For data collection a fractional factorial design of experiments method is employed in three steps. Instead of doing three full factorial designs, a fractional factorial design is used to lower the number of samples required in the first run. Data from a previous design of experiment on the same powder batch but with a different machine combined with gathered information from the literature review [12], [11]

is utilized to determine starting ranges for parameters in the first design of experiment. Each design of experiment will narrow down the range of parameters, illustrated in Figure 16, by ranking of crack density and printability.

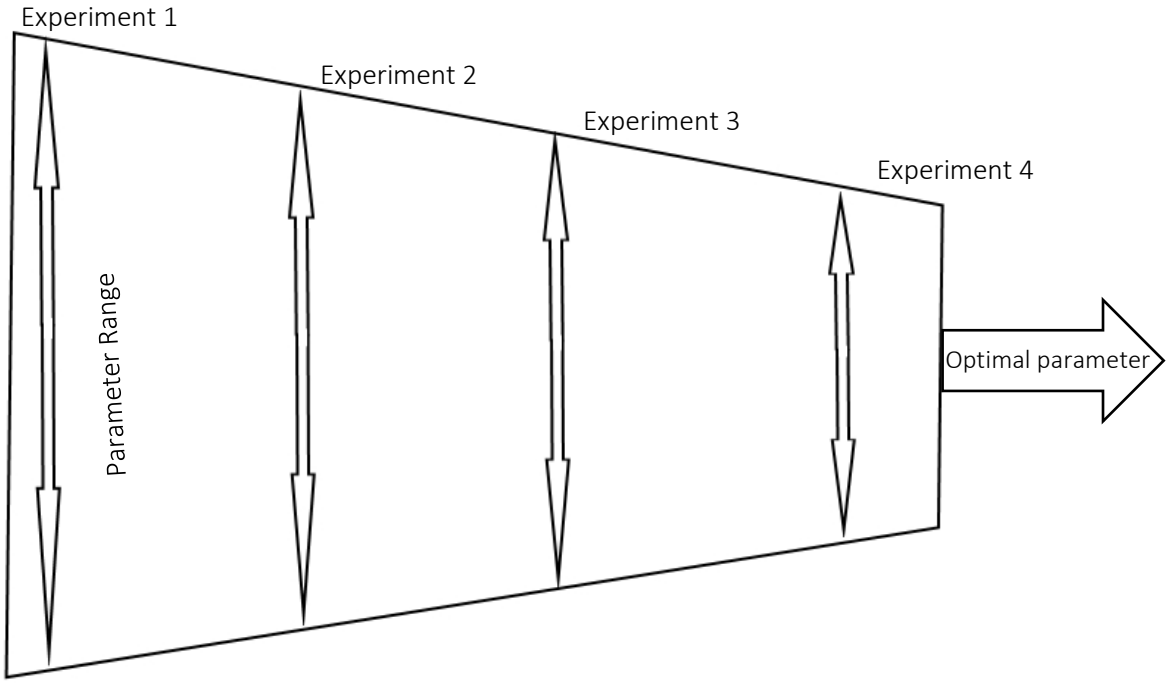

Figure 16. Illustration of how the range for parameters are narrowed down

Using data from all design of experiments an optimal set of parameters is derived and each parameter is evaluated to determine the effect and relation to crack density.

3.3.1 Design of experiment

All samples were printed as 10x10x10 mm cubes, complemented by geometries such as cylinders, and evaluated in an as-printed condition. Equation 7 illustrates, again, how the process parameters are used in the volumetric energy density (VED) method.

$$Volumetric\ Energy\ Density = \frac{Laser\ Power}{Scan\ speed * Hatch\ distance * Layer\ thickness} \quad (7)$$

The laser power is kept above 50 watts since experiments show that even if the energy density is high, 50 watts or less are not enough to fully fuse the powder. Hatch distance should be kept below 0.1 mm according to M. Cloots et al [12]. The layer thickness is kept constant. According to the literature there is a limitation in the suitable energy density range where lack of fusion occurs in the low end and in the high end the material is unprintable. This limitation is used as a requirement when designing the combination of parameters found in Table 5, Table 6 and Table 7. Consequently, the input combination must stay between 40 and 300 J/mm^3 shown in equation 8:

$$40 < \frac{Laser\ Power}{Scan\ speed * Hatch\ distance * Layer\ thickness} < 300\ [\frac{J}{mm^3}] \quad (8)$$

To generate, analyse and create results from the design of experiments the program JMP Pro 13.2 created by SAS were used. In JMP there is a set of predefined DoE's to choose from depending on the experiment and for this experiment a custom design was created. The reason for choosing a custom design was to be able to fully control the DoE and remove sets of parameters that fall outside the

specified range. In JMP the variables are assigned a type depending on their role and how the program should weight, evaluate and assign values for designs.

DoE 1 main purpose was to find the outer process windows while DoE 2 and DoE 3 were used for the optimization process. The three variables (Laser power, Scanning speed and Hatch distance) influence on the response surface was expressed according to second-order equation expressed as:

$$y = \beta_0 + \sum_{i=1}^{k} \beta_i X_i + \sum_{i<j}^{k} \beta_{ij} X_i X_j + \sum_{i=1}^{k} \beta_{ii} X_i^2 + \epsilon \tag{9}$$

Which can be lengthen to visually present how the parameters interact

$$y = \beta_0 + \beta_1 X_1 + \beta_2 X_2 + \beta_3 X_3 + \beta_{11} X_1^2 + \beta_{22} X_2^2 + \beta_{33} X_3^2 + \beta_{12} X_1 X_2 + \beta_{13} X_1 X_3 + \beta_{23} X_2 X_3 + \epsilon \tag{10}$$

Where Y is the response influenced or controlled by the 3 parameters, Laser power (X_1), Scanning speed(X_2) and Hatch distance(X_3). DoE 2 and DoE 3 will be generated according to the Doehlert design matrix which consist of k^2+k+1 number of points shown graphically in Figure 17.

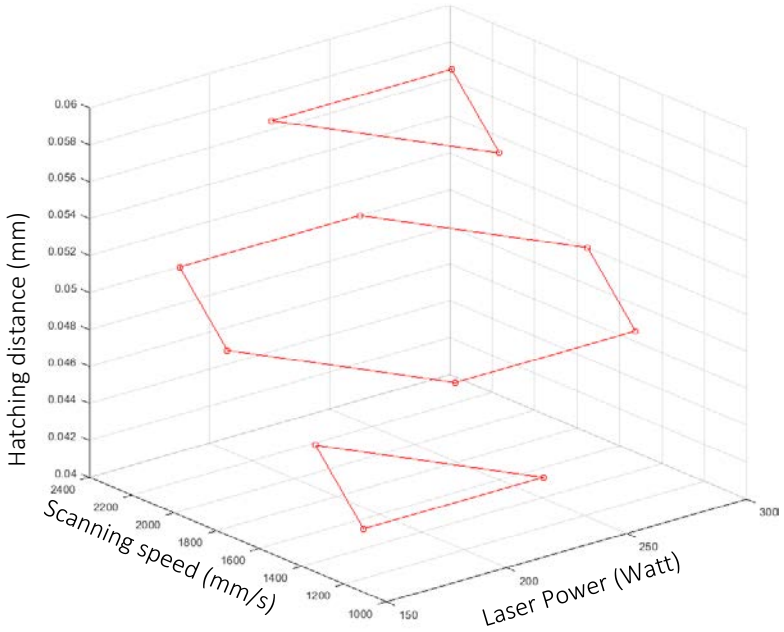

Figure 17. Graphically representation of a Doehlert design matrix.

3.3.1.1 Design of experiment 1

The purpose of the first run of experiments is to narrow down and find the extreme points of variables that the material can handle without a print failure. Table 5 show the range of the variables for experiment 1.

Table 5. Design of experiment 1 parameter range

Design of experiment 1		
Factor	*Type*	*Numeric Range*
Laser power (watt)	Continuous	100-300
Scanning speed (mm/s)	Continuous	1000-1600
Hatch distance (mm)	Discrete	0,04-0,06
Volumetric energy density (J/mm^3)	-	50-300

Since the purpose of DoE1 is to find a suitable parameter range for the material, a lower number of samples needs to be printed. Samples with poor quality and even print failure are expected. A variant of Taguchi's array is used since it explores the extreme points in a fraction factorial design.

3.3.1.2 Design of experiment 2 and 3

DoE 2 is a fractional factorial design with Doehlert matrix design employed which creates an orthogonal projection with the data points in a 3D space, illustrated in Figure 17. The reason for using a fractional factorial design is to lower the number of runs required. Perevoshchikova *et al* [28] did a similar experiment using a Doehlert design matrix with good results. The total number of points for DoE 2 is 14 since there are three variables which gives $3^2+3+1 = 13$ and the 14^{th} point represent the global maximum. Table 6 shows the parameter range used which is derived from the results obtained with DoE 1 both in terms of printability and crack density.

Table 6. Design of experiment 2 parameter range

Design of experiment 2		
Factor	*Type*	*Numeric Range*
Laser power (watt)	Continuous	150-300
Scanning speed (mm/s)	Continuous	1000-2500
Hatch distance (mm)	Discrete	0,04-0,06
Volumetric energy density (J/mm^3)	-	75-250

The third and final DoE is derived from the results of DoE 2 and narrowed down even more. The same design matrix is used as in DoE 2 but with a lower range for the variables. Table 7 below show the parameter range used for DoE 3.

Table 7. Design of experiment 3 parameter range

Design of experiment 3		
Factor	*Type*	*Numeric Range*
Laser power (watt)	Continuous	175-225
Scanning speed (mm/s)	Continuous	1600-2200
Hatch distance (mm)	Discrete	0,04-0,06
Volumetric energy density (J/mm^3)	-	90-150

The matrices for the three DoEs can be found in Appendix A:1,Appendix A: 3 and Appendix A: 6 respectively.

3.3.1.3 Evaluation of design of experiments

JMP, the program used for designing the experiments, have built-in tools for analysing data and evaluate the response surface model. To assure a good validity of the results there are three statistical parameters that will be in focus of this study.

- R^2 which is also known as 'coefficient of determination' and is a measurement of variation. R^2 takes a value between 0 and 1 where values close to 1 indicates a good model fit. At values close to 0, the model fit is unsatisfactory and the predictive effect is inconclusive. If $R^2 = 0$ the prediction is no better than the mean response.

- *Analysis of variance*, or F-ratio in JMP, compares the means of a random set of samples and determines the predictive capabilities of the model by comparing the mean of several samples, or populations. A large F-ratio indicates that some interaction between factors are captured and that the variance is not due to chance.
- *Lack of fit* is a direct measurement of how effectively a regression model describes the correlation between factors and response. Lack of fit occurs if there are missing interactions between factors in the model. In JMP a small *Prob>F* value indicates that important interactions between parameters are missing and lack of fit is present.

3.3.2 Melt pool measurements

To reveal the full shape and size of the melt pool, a cross section from the last layer is examined by cutting the samples parallel to the last scanned line as shown in Figure 18. The samples are electrolytically etched with Oxalic acid using a voltage of 3 Volts to reveal the solidification structure.

Figure 18. Samples are cut parallel to last scanned line, parallel to the line.

Measurements are taken at random positions along the sample top surface to get a good representation of the entire sample. Pictures are taken at 20x magnification with light optical microscopy and the depth and width of melt pools are manually measured within the imaging software. Figure 19 show the melt pools and how the measurements is performed where only half of the melt pool width is measured due to overlapping. In total 21 measurements per samples were performed to get the average values on the melt pool.

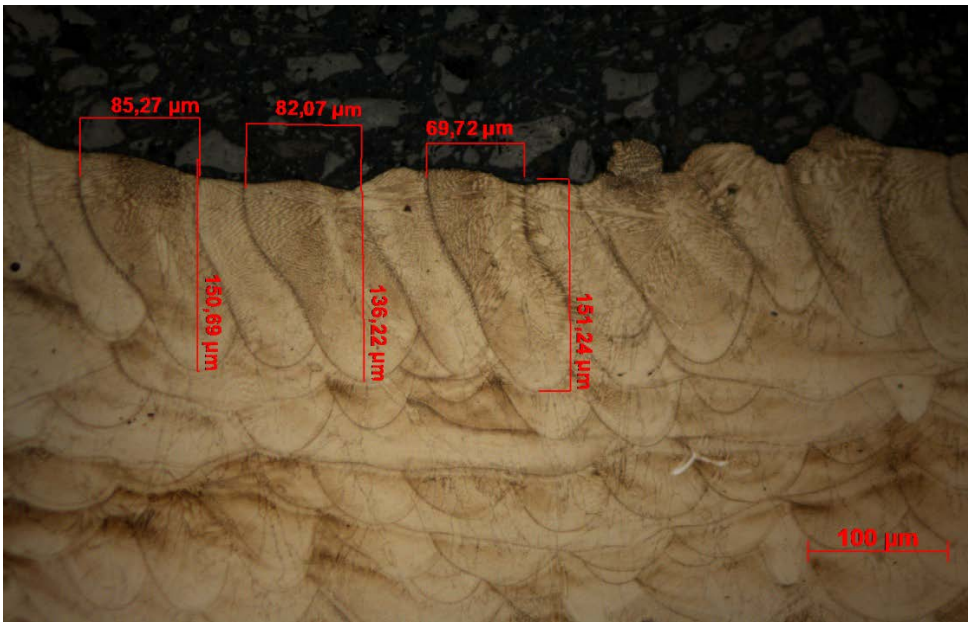

Figure 19.Illustration of the melt pool measurements

The melt pool analysis will focus on two main parts, the first is to measure, analyse and correlate LPBF process parameters with shape and size of the melt pool from the two first design of experiments. These data are used to create a model for predicting the melt pool characteristics which is then verified by the last design of experiment. The model is created by fitting a suitable curve to the obtained data.

3.4 Sample preparations

Cubes of 10x10x10 mm in size were created for the design of experiments as an STL file using Materialize Magics and sliced in the EOS software, RPTools and produced in an EOS M290. Placement of samples on the build plate were done in such a way that the gas flow would not contaminate samples downstream due ejected particles carried by the flow. Samples were rotated so that only one edge would coincide with the recoater blade when a new layer of powder is applied. The cylindrical test bars that were HIPed and heat treated were prepared like the cubes for the metallographic examination. The cylindrical bars were grinded before HIP and heat treatment to remove any surface defects that could act as a nucleation sites for cracks.

Printed samples were removed from the build plate by wire cutting. The samples were cut to reveal the cross-section in build direction (Z) and perpendicular to build direction (XY) as shown in Figure 20 below by a rotary disc. For the sample cubes, the last printed layer is used to examine the melt pools.

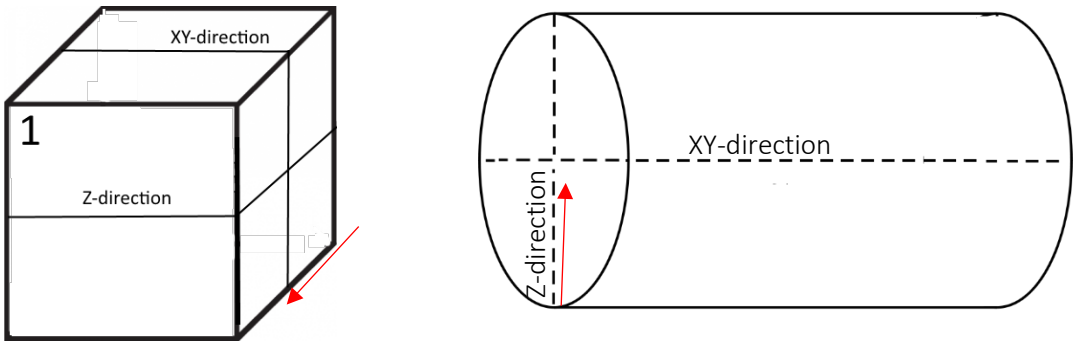

Figure 20. Samples cut in Z- and XY-direction

After cutting, the samples were mounted in resin, grinded and polished as preparation for light optical microscopy. Grinding were performed in steps with grinding grade 120->220->500->1200 after which they were polished with diamond paste of 3 µm and finally 1 µm.

3.5 Defect density

The defect density measurements were performed according to ASTM E2109-01 standard which specifies the required magnification, number images etc. The samples and imaging were divided into XY- and Z-direction to be able to distinguish any difference in defects from build direction.

Images were converted from the HD camera's RGB to binary. This will show all defects as black features while everything else is white. By knowing the scale, that is assigning each pixel with a unit of length, the total area, length, shape etc. of the defect is measured in the program ImageJ. This process is illustrated in Figure 21. All pictures are taken randomly across each sample and the examined area covers roughly 25% of the total area to give a good statistical reliability since the defect density is homogenously distributed across the material.

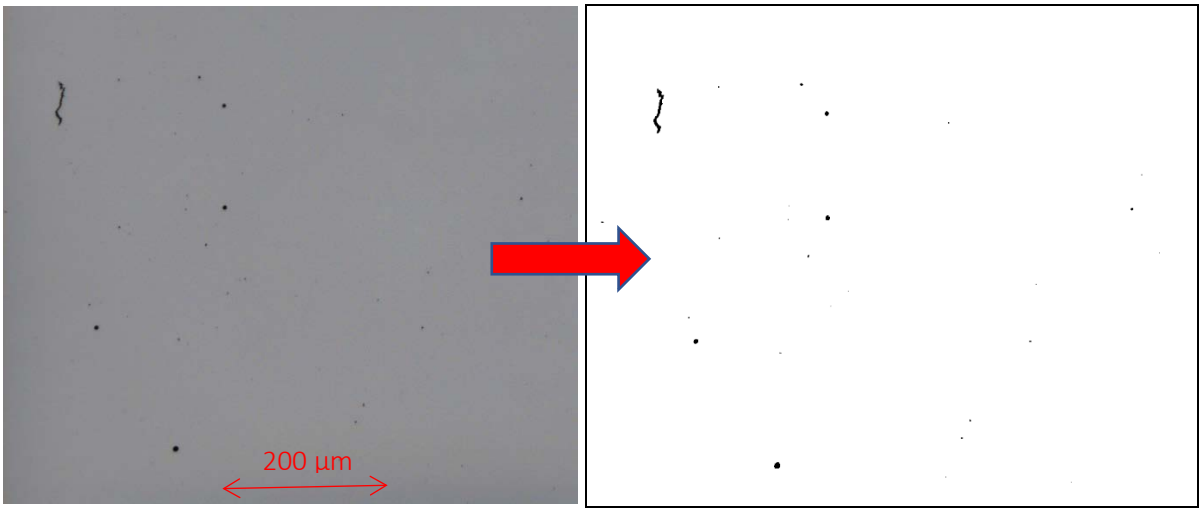

Figure 21. An RBG images is transformed to Binary to outline the defects.

Defects that adds up to the total defect density are pores, lack of fusion and cracks, where cracks are of main interest. By filtering by ferret size (the longest possible distance between two points within a boundary) and roundness cracks can be filtered out. Pores have high roundness and low ferret size while cracks have low roundness and high ferret size, Figure 22.

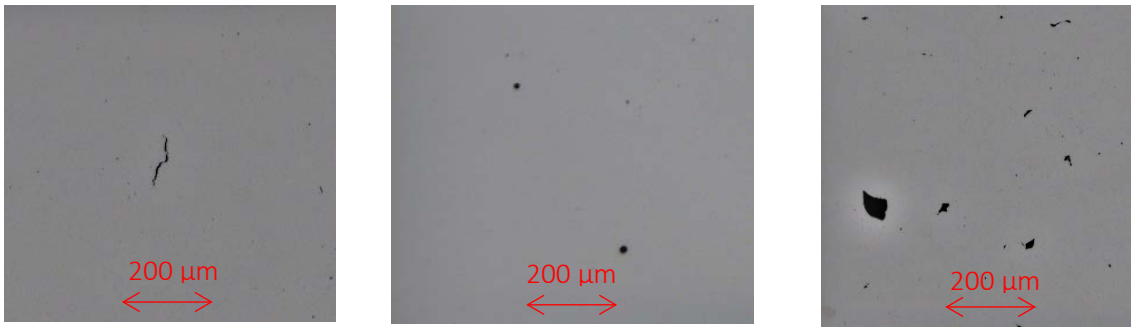

Figure 22. The three kind of defect present. Left: micro cracks. Middle: Pores. Right: lack of fusion

The filter setting used is: everything below 1.5 µm is regarded as noise and is not included. Cracks have a roundness of < 0.5 while pores have > 0.5. Due to the measurement resolution cracks with a Ferret size of > 5 µm were disregarded. Cracks have a roundness of < 0.5. If samples had lack of fusion they were removed from the analysis.

3.6 Hot isostatic pressing

The samples were HIPed at Quintus Technologies in Västerås and all parameters used for the HIP process were developed with the help of their expertise. Figure 23 shows a HIP machine similar to the one used for this project. This machine makes it possible to precisely control the temperature, heating rate and pressure and enables the possibility to integrate the heat treatment into the HIP cycle. Furthermore, heat treatment under pressure should supress the strain age cracking. A shorter post processing cycle can increase productivity and making it more economical to employ additive manufacturing.

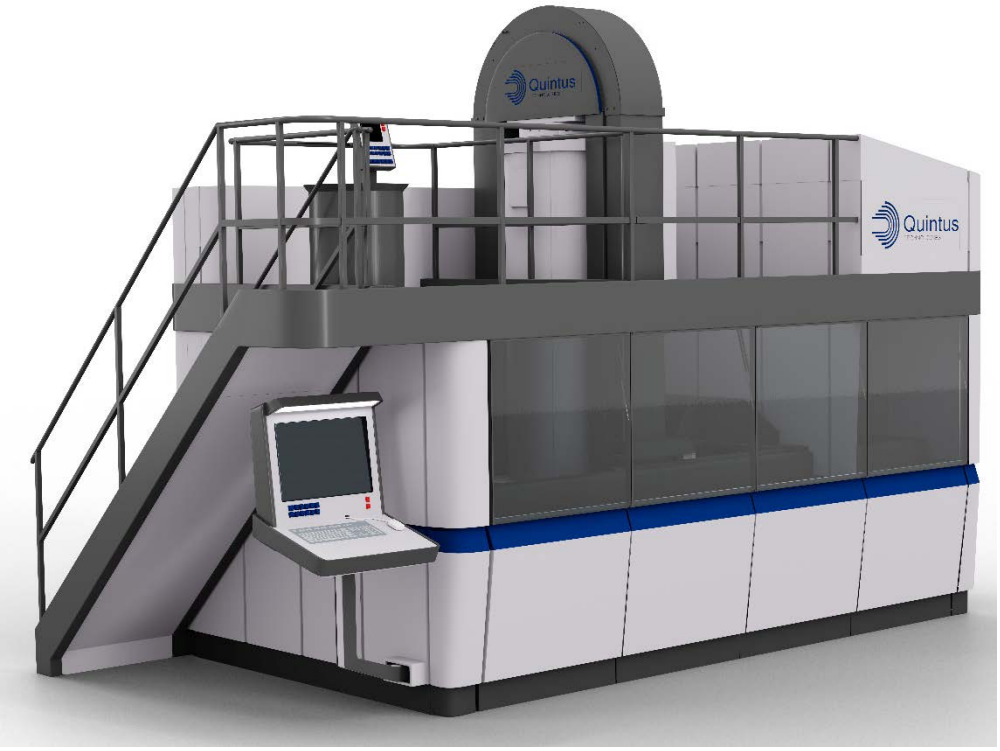

Figure 23. Hot isostatic machine. Courtesy of Quintus Technologies

3.6.1 Effect of Hot Isostatic Pressing

HIP densification was evaluated by measuring crack density in samples after HIP cycles with varying temperature and pressures. To investigate crack opening during heat treatment on post-HIP samples, heat treatment was performed in the HIP machine under pressure, as well as in traditional furnaces. To ease evaluation on the effect of the hot isostatic pressing process, a higher defect density then what was found from the design of experiments is needed. For this reason another itteration of powder with similar composition but with a higher crack density was utilized. The HIP parameters and subsequent heat treatment are shown in Table 8.

Table 8. HIP and Heat treatment parameters.

HIP-temperature (Celsius)	HIP-pressure (Bar)	HIP-time (hours)	HT-temp (Celsius)	HT-press (Bar)	HT-time (hours)
1210	1000	4	None	None	None
1210	1000	4	850	0	2
1210	1000	4	850	1000	2
1210	2000	4	None	None	None
1210	2000	4	850	0	2
1210	2000	4	850	2000	2
1000	1000	4	None	None	None
1000	1000	4	850	0	2
1000	1000	4	850	1000	2
1000	2000	4	None	None	None
1000	2000	4	850	0	2
1000	2000	4	850	2000	2

3.6.1.1 Hot isostatic pressing + heat treatment temperature profile

Some samples from the first HIP cycle showed a substantial amount of macro cracking that stretched along the samples, in a transversal direction and extended radially into the sample. To solve or mitigate macro cracking the heat-treating cycle including temperature, hold time and heating rate is tailored based on literature study, existing standards and simulations using JmatPro to determine the γ' formation range. Tests performed to evaluate and validate constructed heat treatment cycles were performed in a ceramic tube furnace and the final heat treatment was performed in the HIP with applied pressure. Since strain age cracking occur during heating it is beneficial to increase the pressure in the HIP before the heating starts. This supresses crack formation and also enables a higher heating rate than what is possible in a traditional furnace due to the increased density and thermal conductivity of the gas. Figure 24 shows the constructed heating strategy compared to the actual heating obtained from the data logs in the HIP machine as is shown in Figure 25. The actual heating rates is close to the formulated one. Figure 25 also shows that the pressure is increased before heating occurs.

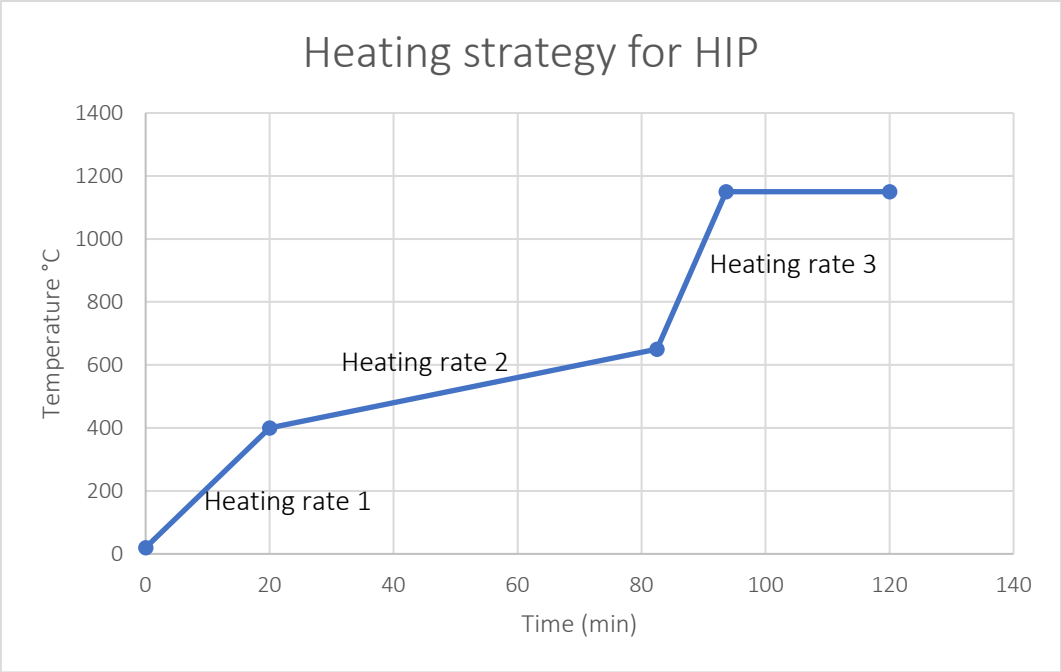

Figure 24. Constructed heating strategy

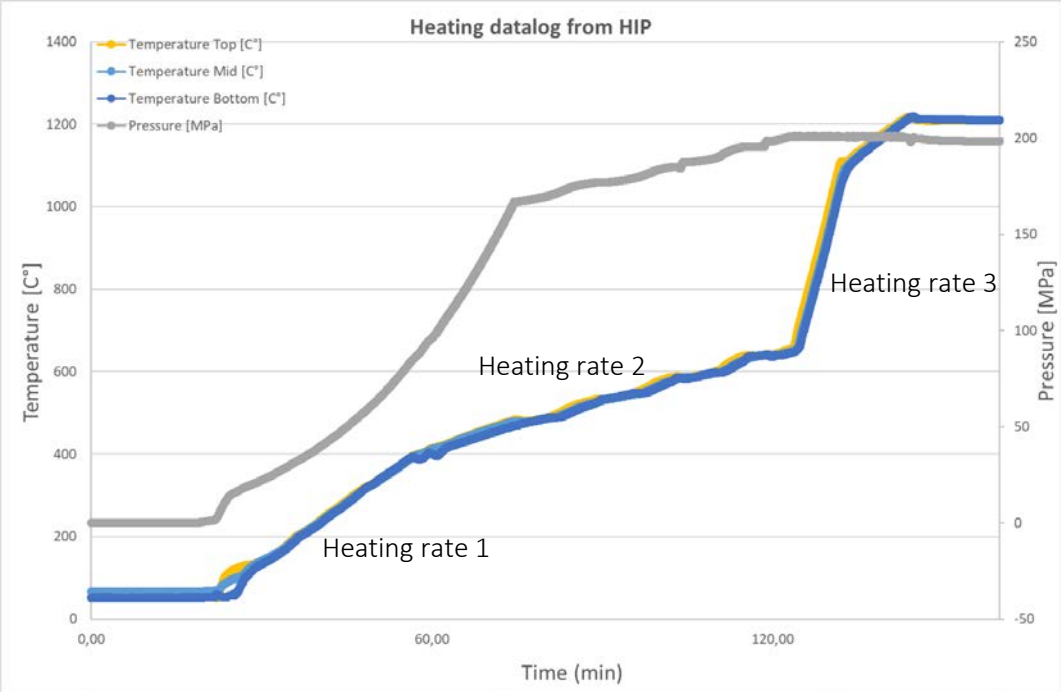

Figure 25. Heating rate obtained from the data logs

3.6.1.2 Evaluation of defect density post-HIP

Crack density after HIP was analysed in the same way for as as-built samples i.e. by image analysis, following the procedure in 3.5. However, images acquired using optical microscopy cannot distinguish between pores and oxide as both have similar geometries and appear black in a light microscopy. Scanning electron microscopy (SEM) together with energy dispersive X-ray spectroscopy (EDX) attached to SEM that allows to qualitatively measure the chemical composition, was employed to investigate the nature of any residual defects in post-HIP samples.

3.6.1.3 Grain size measurements

As part of evaluating the effect of HIP on LPBF manufactured parts is the analysis of the microstructure. Both shape and size of the grains will be affected by HIP and heat treatment. The main goal was to compare the grains of samples that are HIPed with different parameters to determine optimal HIP + HT conditions. Grain size measurements were performed according to ASTM E112-13 standard which specify in detail how the measurement is performed. The images used for the grain measurements were taken by a FEG-SEM using the backscattered electron detector. ASTM E112-13 was used to determine the homogenisation of HIPed and heat-treated samples by comparing measured grains to the specified standard.

4
Results

In this chapter, relevant results obtained from the experimental part are presented as clear as possible. Only the most relevant figures and tables are presented in the report with the appendix as compliment.

4.1 Results from Design of experiments

The first DoE is created with Taguchi's method, since this method only requires 9 different experiments, to get a broad overview of the responses from the parameters. After the experiment from Taguchi´s method a Doehlert matrix was used to create parameters for the second and third experiment. Doehlert matrix was chosen because it is easy to expand the matrix in the direction that is most promising, i.e. the design parameters for DoE 3 can be based on DoE 2 and both can be used together in the main analysis.

4.1.2 Parameters and defect density

For all DoEs, samples that were in the low end of the specified energy density range showed lack of fusion. The transition VED was found to be around 80-90 J/mm^3 and laser power seems to be the major factor. In the high end of the specified VED range there is risk of failed prints. The surface becomes rough due to turbulence and evaporation mixed with sparks that causes particles to jump. Sparks can contaminate surrounding areas which also increase the risk of recoater blade hitting the samples, even small contamination can cause a build-up of a rough surface which increases as the number of layers increases. The rough surface and failure of print seems to happen above 200 J/mm^3 but with a large range depending on the laser exposure time, or scanning speed.

4.1.2.1 Design of experiment 1

The design matrix data is shown in Appendix A:1.

Sample 7 and 8 failed due to excessive melting causing a rough surface which the recoater blade hit. Sample 1 failed due to sputtering, i.e. when particles from nearby samples landed on the surface. Sample 2 and 3 had to low energy density which led to lack of fusion as shown in Figure 26.

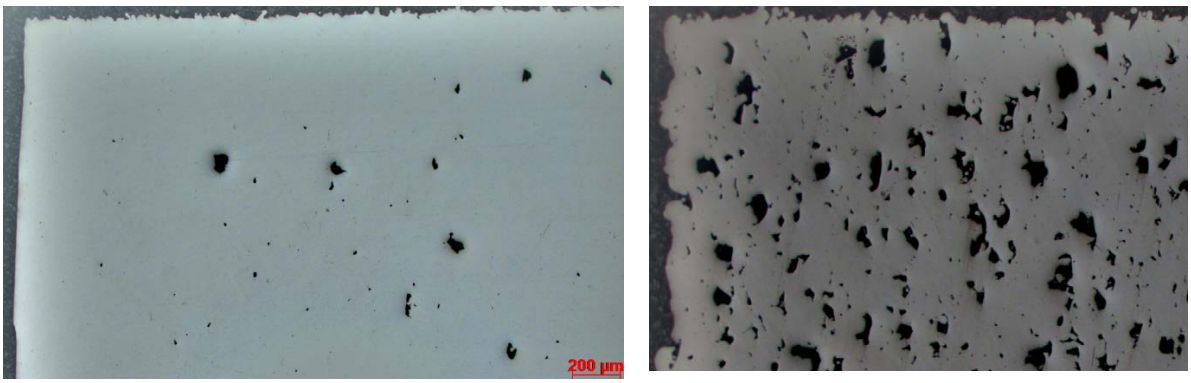

Figure 26. Sample 2 and 3 showing substantial lack of fusion.

Failed print is typically observed if there is too high energy density (especially laser power), which is true for sample 7 and 8 while samples 1 was aborted due to semi molten particles from other samples sputtered into the already scanned area and thus created irregularities which touched the recoater blade. The crack density from DoE 1 is shown in Figure 27 and all results can be found in Appendix

A:2. Samples that failed during print or had lack of fusion is excluded. As shown in Figure 27, there is no clear correlation between the crack density and process parameters or VED. Furthermore, the crack density is very low even for samples with the highest amount of cracks.

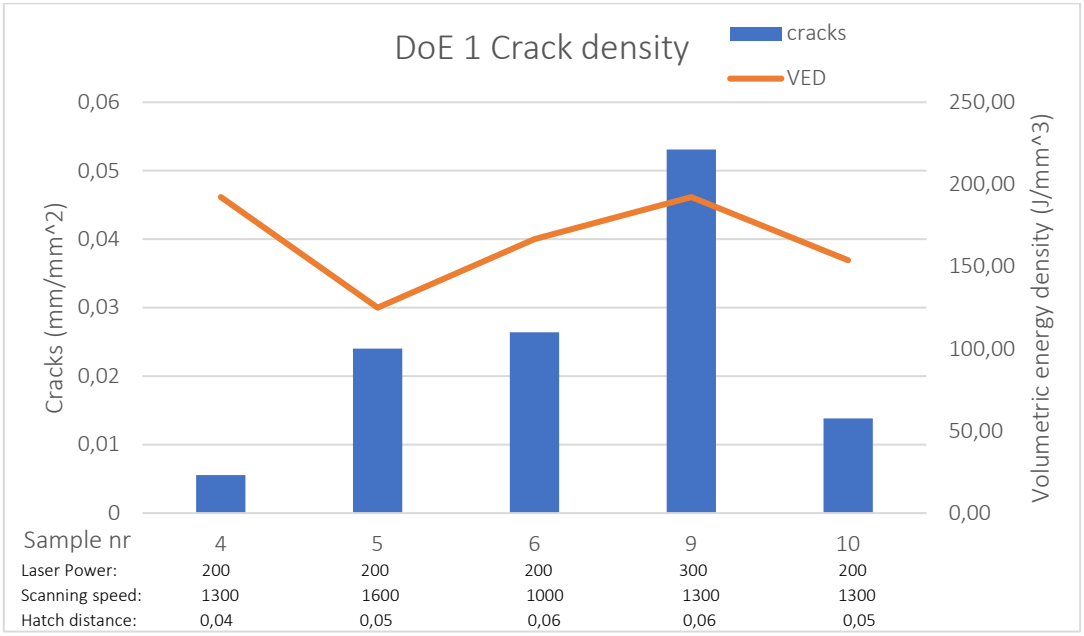

Figure 27. Crack density from DoE 1. Laser power in watts, Scanning speed in mm/s and hatch distance in mm.

Sample 4 and 9 had a remarkable difference in crack density even if the overall density is low. However, as shown in Figure 28 there is only a small difference in number of cracks. On average there is only one crack per image in sample 9 while sample 4 was more or less crack free.

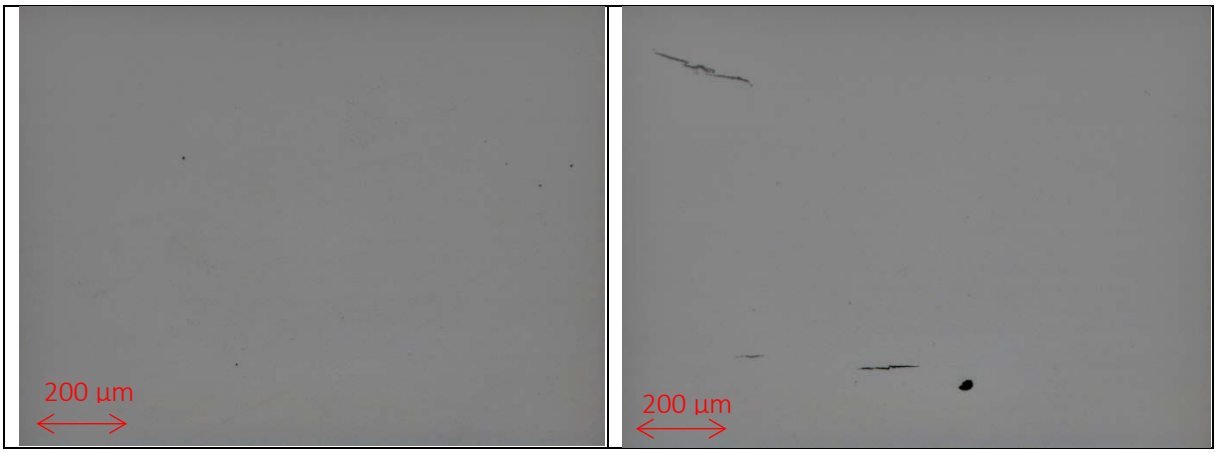

Figure 28. Comparison between sample 4 and 9. Left: Sample 4. Right: Sample 9

4.1.2.2 Design of experiment 2

In DoE 2 all samples were printed successfully but there was a rough surface on samples with high energy density which caused the recoater blade to touch the top surface. Even if the crack density were low in these samples, they were considered a no-go. The resulting parameter matrix for DoE 2 are shown in Appendix A: 3.

For all samples the cross-section of XY plane were compared to Z-, or build-, direction. Generally, no significant difference in defect density between XY and Z direction was found. Figure 29 below show sample 1 and 4 in both XY and Z direction.

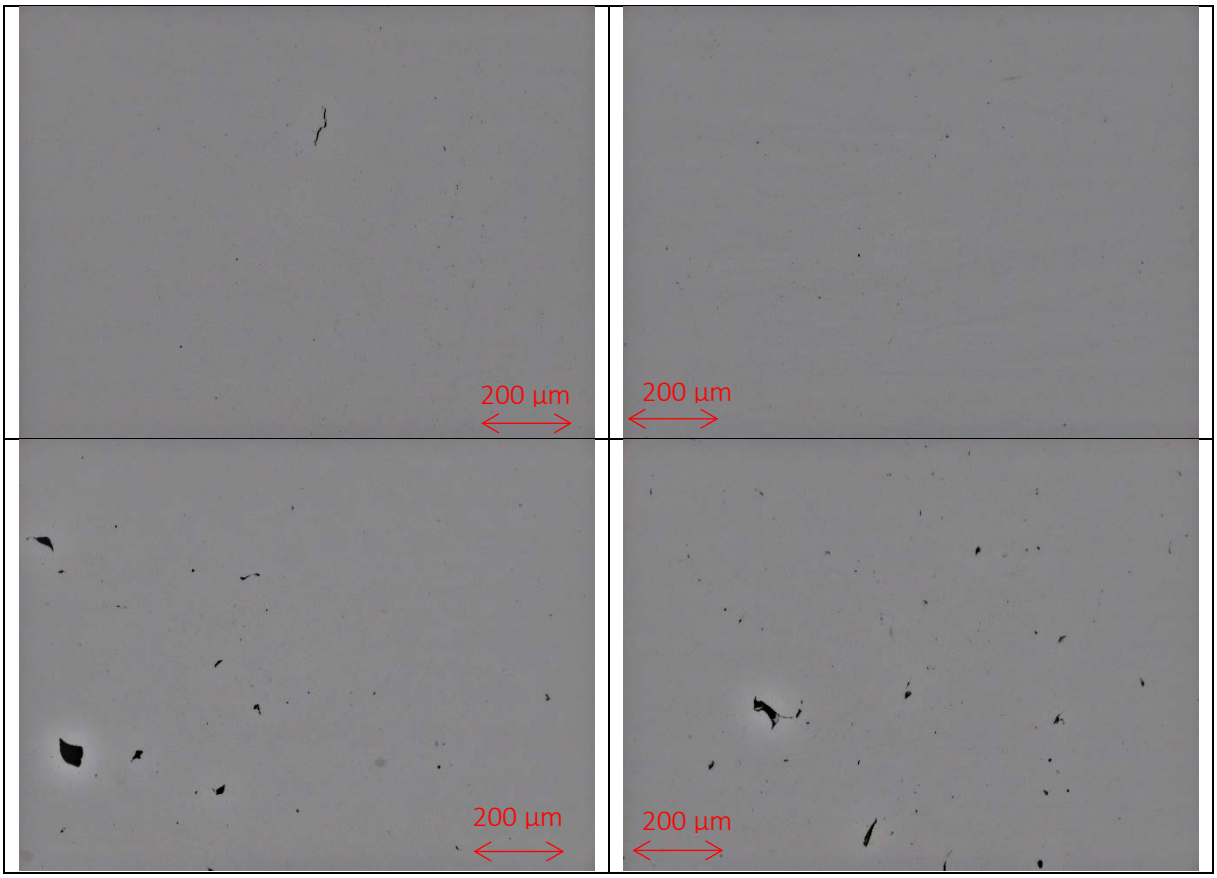

Figure 29. Design of experiment 2, comparison between Z- and XY direction.
Left: XY direction. Right Z direction.
Top: Sample 1. Bottom: Sample 4.

Even at the extreme points in, there were no samples with significantly high total crack density compared to the more moderate experimental parameters, as has been observed by M. Cloots, P. et al [12]. Figure 30 shows crack density data for all the samples from DoE2. All results from DoE 2 can be found in Appendix A:4.

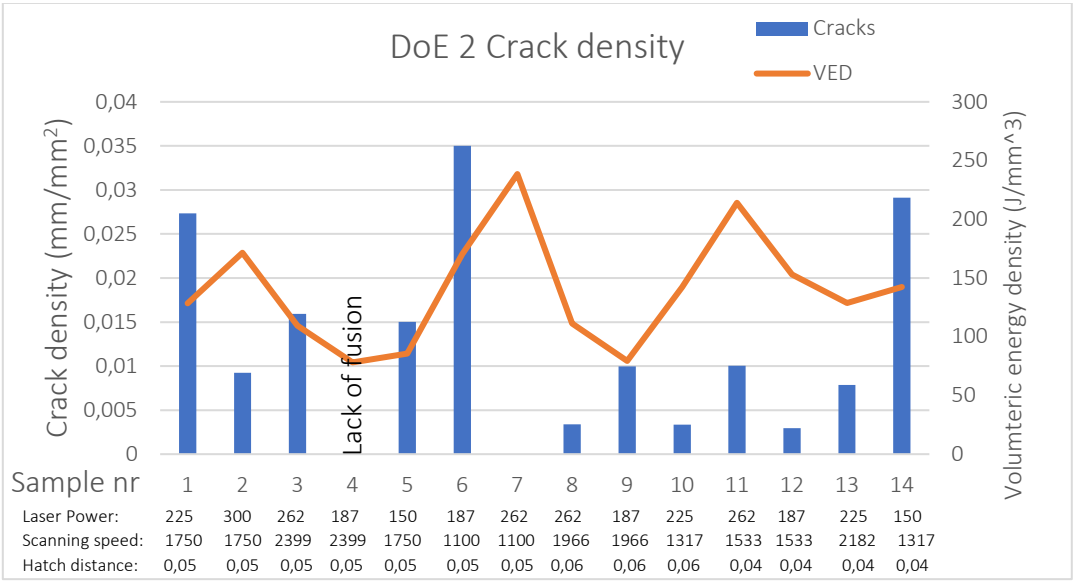

Figure 30. Crack density from DoE 2. Laser power in watts, scanning speed in mm/s and hatch distance in mm.

As shown in Figure 30, even in the worst samples there is a low crack density when comparing to previous tests with similar material and powder properties. However, compared to DoE 1, the average crack density as well as the spread is lowered. The average number of cracks per images is less than one for DoE 2. As in DoE 1, some sets of parameters in DoE 2 resulted in sputtering, balling or irregular surfaces. These parameters are considered as a no-go even if they produce a sample with low crack density. One example is sample number 7 that had a very low crack density but were almost unprintable. Sample 4 showed significant lack of fusion and thus is removed from the analysis, in total 6 samples were deemed unsuited for further use in DoE 2. Figure 31 show a top view of how samples that are deemed unprintable behave during manufacturing as well as the surface topology for three samples. Reason for bad printability is because the recoater blade hits the samples surface, sputtering occurs or a rough surface.

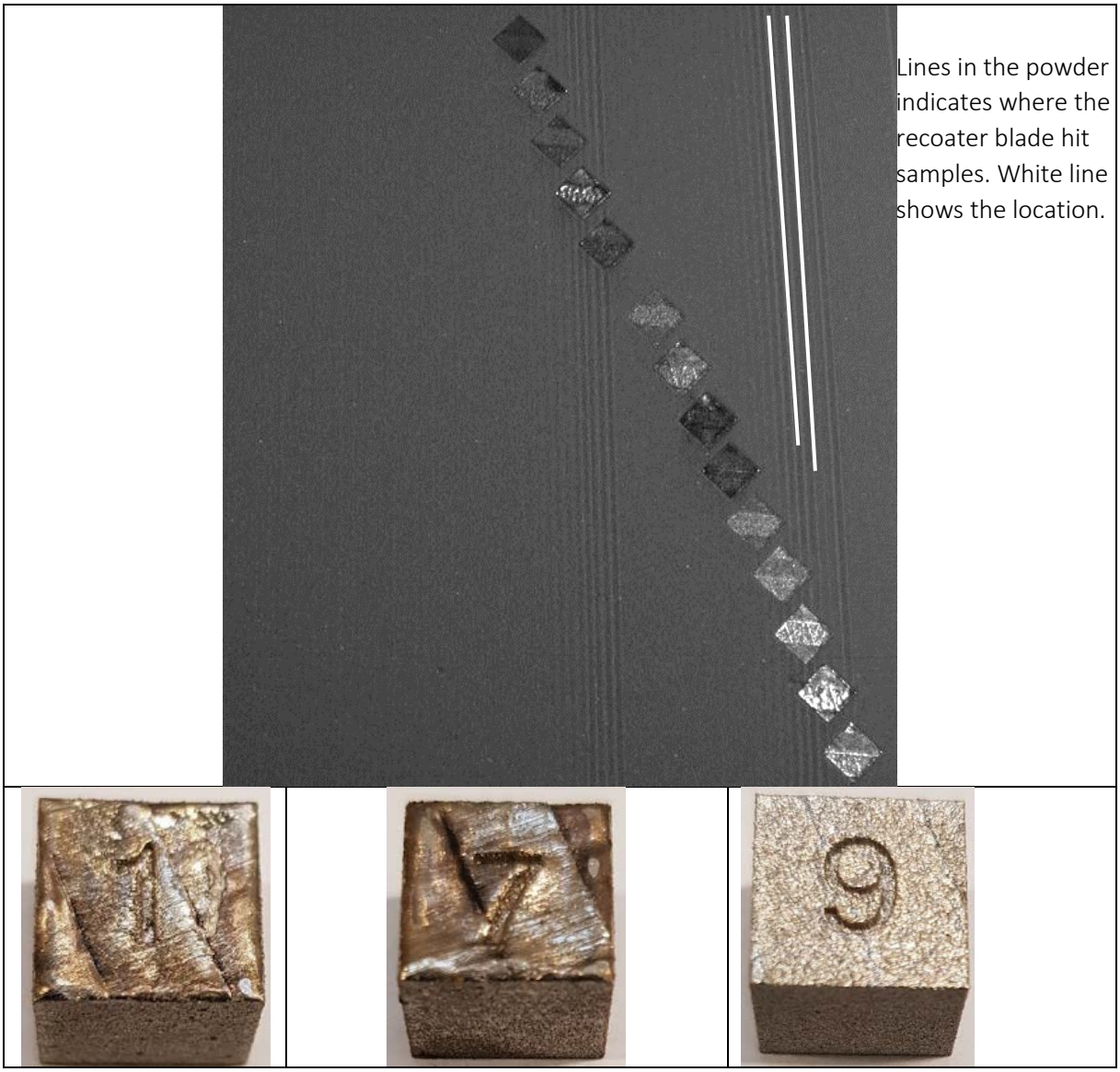

Figure 31. Top: Top view of the printing chamber, sample number from bottom to top is 1-14. Bottom: Surface roughness of different samples

4.1.2.3 Design of experiment 3

The final set of parameters was created from the results from DoE 2 with focus on lowest crack density while printability and pore density had lower priority. Also, sample parameters that show signs

of keyholing or deep melt pools that are close to keyholing were avoided. Appendix A: 6 show the parameter used for DoE 3.

There was no indication from the first DoE that an increase in speed would affect crack density if the loss in VED were compensated for, within the specified interval, with an increase in laser power. Thus, the scanning speed was increased for DoE 3. All samples from DoE 3 was printed successfully with a smooth surface. Figure 32 show the resulting crack density, all results can be found in Appendix A:7.

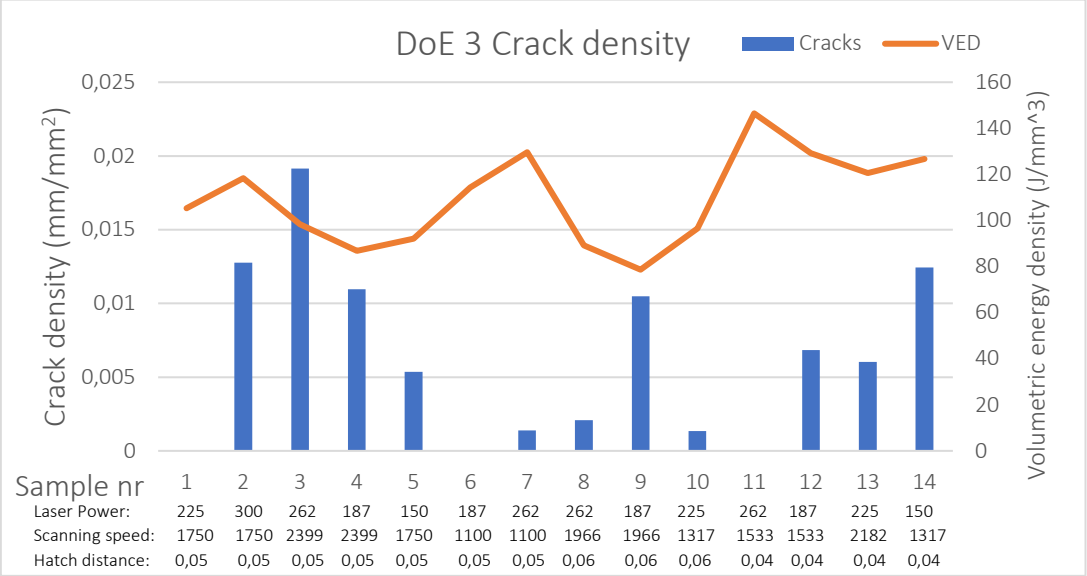

Figure 32. Crack density from DoE 3. Laser power in watts, scanning speed in mm/s and hatch distance in mm.

As shown in Figure 32 the total average crack density is even lower compared to DoE 2. However, as in both DoE 1 and DoE 2 there is no clear indication to what is affecting crack density. For example, sample 1 and 2 have similar VED, with same hatch distance and scanning speed but varies greatly in crack density. DoE 3 have a higher average laser power and scanning speed then DoE 1 and DoE 2 a lower crack density.

4.1.3 Results of DoE optimization.

In this project a large number of samples were examined in a broad process window. By using all the collected data points for the main analysis, a more accurate model can be found and this was one of the reasons for choosing the Doehlert matrix since it allows easy expansion of the design and old trials can be reused. Figure 33 shows the predicted plot with the red area being the spread of accuracy i.e. the acquired coefficients for the response surface can be used to predict the data points within the red area. It does not cover all the data points and is only valid for certain ranges, shown in Table 10.

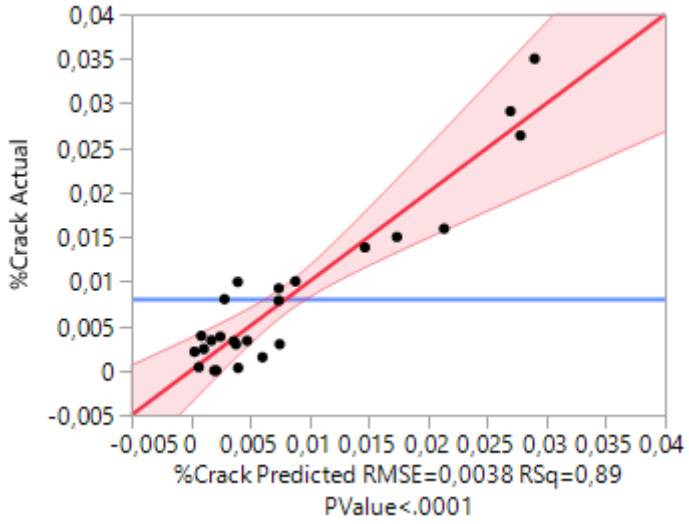

Figure 33. Prediction accuracy plot using the three parameters from JMP

Table 9 shows the full summary of fit and Analysis of variance generated by JMP. With a total of 28 points the prediction has an accuracy of $R^2 = 0.89$, the high F-ration indicates that vital interactions between factors are captured but a low Prob>F indicates that there is a significant lack of fit. The reason for a significant lack of fit could be the small spread in crack density. The resulting coefficient for the response surface equations are shown in Appendix A:10.

Table 9. Summary of fit and Analysis of variance generated by JMP for the main analysis using all available data.

Summary of Fit

RSquare	0,89
RSquare Adj	0,83
Root Mean Square Error	0,0038
Mean of Response	0,008
Observations (or Sum Wgts)	26

Analysis of Variance

Source	**DF**	**Sum of Squares**	**Mean Square**	**F Ratio**
Model	9	0,00200131	0,000222	15,0949
Error	16	0,00023570	0,000015	**Prob > F**
C. Total	25	0,00223701		<,0001*

By plotting the response surface as an isotherm with scanning speed and laser power as the two continuous factors at the discrete levels assigned to the hatch distance there appears to be domains or areas that are prone to cracking. With this contour plot it is possible to find a range for a tolerable crack density and the domain will specify which scanning speed and laser power is acceptable for different levels of hatch distance. The resulting total contour domain are shown in Figure 34 which shows that hatch distance affects the allowed range of laser power and scanning speed and not the crack density. The entire response surface is found in Appendix A:8 and the residual by predicted plot in Appendix A:9

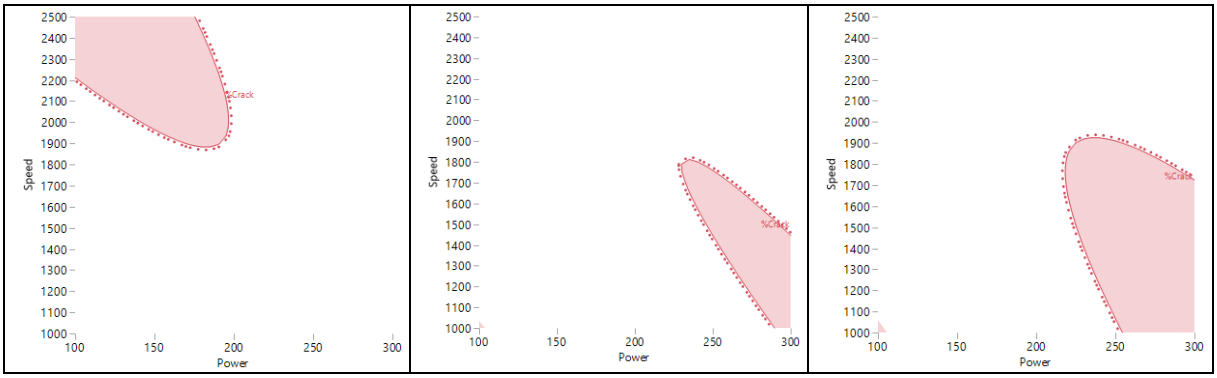

Figure 34. Domain where micro cracks are most likely to happen. All available data used. Left: Hatch distance = 0.4. Middle: Hatch distance = 0.5. Right: Hatch distance = 0.6

Finally, the effect of parameters is shown in Table 10 below which indicates that a mix of laser power and scanning speed is the primary factors affecting crack formation in the range of 1000-2500 mm/s and 150-300 watts.

Table 10. Parameters weight on micro cracks formation generated by JMP. HD = Hatch distance

Source	Worth	PValue
Speed(1000,2500)	5,848	0,00000
Power*Speed	4,517	0,00003
Power(100,300)	3,181	0,00066
Speed*Speed	2,621	0,00239
Power*Power	2,612	0,00245
Power*Hd	1,998	0,01005
Hd	0,174	0,67009

It should be noted that the measured crack densities in all samples evaluated in the process optimization part of this study were generally very low, indicating that the used material is comparably robust against hot cracking over a relatively wide range of process parameters. Therefore, regarding possible correlations between crack density and process parameters, the results from this part can only be used as an indication of effect, even if there are a good statistical support that the performed experiments are more than coincidence. More extreme points are needed for a better fit in the prediction. However, it is seen that by applying a three stage DoE, it was possible to identify the process window for production of more or less defect free samples.

4.2 Melt pool measurements

According to the literature review, melt pool characteristics plays an important role in formation of hot cracks. Keyholing should be avoided since the deeper groove can create a high amount of residual stresses which may cause rise to micro cracks.

4.2.1 Melt pool characteristics

Three distinct shapes or geometries are found for different ranges in width-to-depth ratio or melt pool depth. The three distinct geometries are a shallow ellipse, deep ellipse or keyhole where the transition between shallow and deep ellipse is when width-to-depth ratio is between 1,2-2, whereas a transition between a deep melt pool and keyhole is not as easy to distinguish. One feature unique to the keyhole effect is the plateau before a deeper groove appear. The geometries are shown in detail in Figure 35.

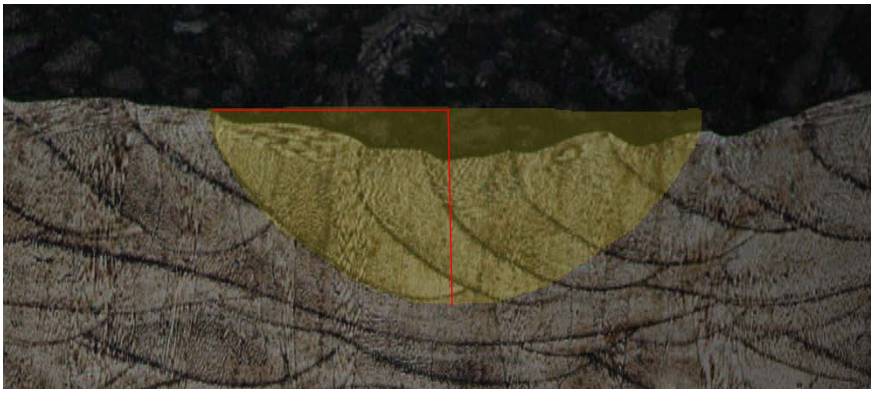

A shallow melt pool can be compared to a ellipse where the major axis is horisontal.

The transition between a shallow and deep melt pool is charactrised by a circular shape, both the major and minor axis are roughly equal.	
Deep melt pools have a vertical major axis.	
The keyhole geometry have a plataeu followed by a deeper, narrower second grove.	

Figure 35. Melt pool characteristics. The three melt pool geometries observed in the samples.

4.2.2 Melt pool results

It is found that keyholing occurs in all three designs of experiments. However, DoE 1 and DoE 2 had a more frequent occurrence than DoE 3. Usually keyholing occurred in samples with higher volumetric energy density, either high laser power or low scanning speed. The most probable reason for this behaviour is that it requires extra time or energy to penetrate a deeper section of the material. Appendix B1 show measured melt pool depth, half the width and width-to-depth ratio for DoE 2.

A higher power will give a deeper melt pool while increasing the scanning speed decreases melt pool depth. Hatch distance does not seem to affect the melt pool. Figure 36 show how power and speed correlates to melt pool depth. A high ratio of Power/scanning speed means that there is a higher energy input and a deeper melt pool is formed while a lower ratio means the opposite. All data used can be found in Appendix B2.

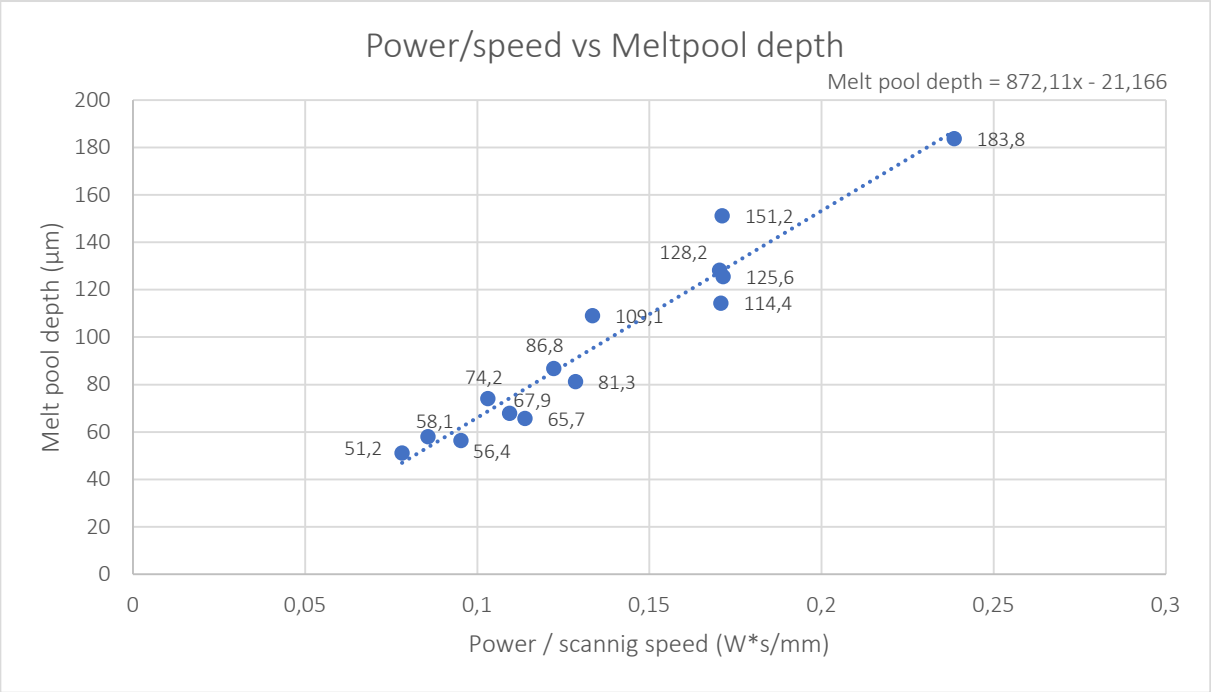

Figure 36. Prediction model for melt pool depth.

The model to predict the melt pool depth and width-to-depth ratio is produced from design of experiment 2. The Vertical ellipse shape or deep melt pools is usually close to form a keyhole geometry and sometimes there is a mix of deep melt pools and keyholes. The model used to predict the melt pool depth, which can be correlated to the geometry, is a linear equation obtained by fitting a line to the data points. Table 11 summarizes the results from the measurements on the melt pool for DoE 3 and predication made all values are averaged, se Appendix B3 for the full table.

Table 11. Melt pool prediction compared to actual values. Measurements In µm.

Measured values		Predicted values			
Depth	Width:Depth ratio	Predicted depth	Predicted width:depth	Prediction error depth	Prediction error Width:depth
68,4	2,07	71,6	1,91	6%	13%

The melt pool depth prediction was more accurate than the melt pool depth-to-width ratio. However, it is mostly the depth-to-width ratio that is used in literature. However, since keyholes is usually followed by a deep melt pool and there is a clear correlation between keyholing and depth the model holds up. In Table 12 are the range listed were the three geometries were found with the minimum and maximum value in the range.

Table 12. Summary of the melt pool characteristics and in which range the different shapes are found.

MELT POOL WIDTH: DEPTH			MELTPOOL DEPTH (µM)	
SHAPE	Range min	Range max	Range min	Range Max
KEY HOLE	1,27	2,0	114,4	183,8
VERTICAL ELLIPSE	1,66	2,20	74,2	125,6
HORIZONTAL ELLIPSE	1,74	2,39	51,2	67,9

Figure 37 show that adding DoE 3 measurements only slightly affect the formulated linear equation.

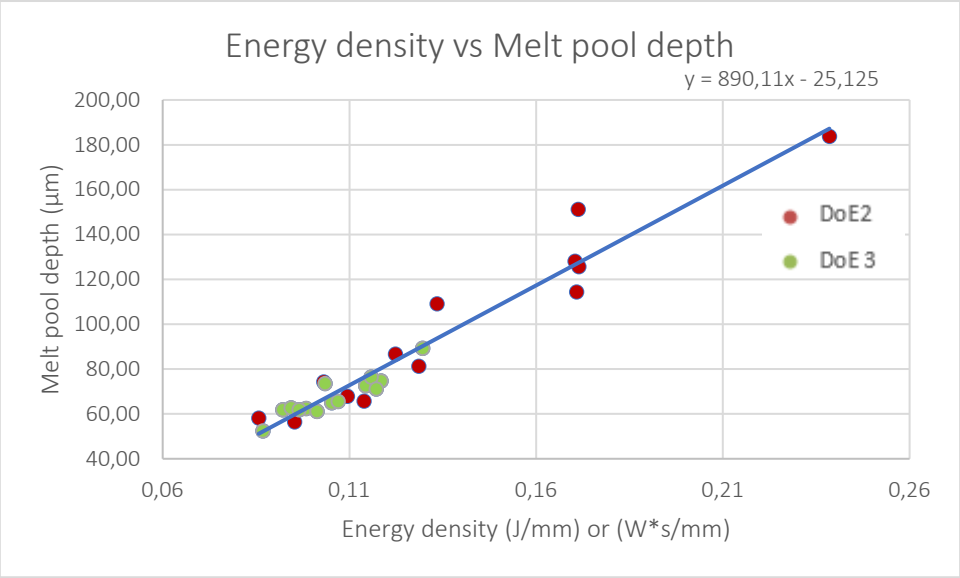

Figure 37. Final melt pool model with all available data added.

There was no indication that key holing, depth or width-to-depth ratio affected crack formation for this material. Figure 38 shows the depth-to-width ratio and crack density with marked zones for the three shapes of the melt pool, no significant variation is found between the three shapes. It is shown in earlier works regarding welding, including additive manufacturing, that controlling melt pools are a vital part of a reducing cracks.

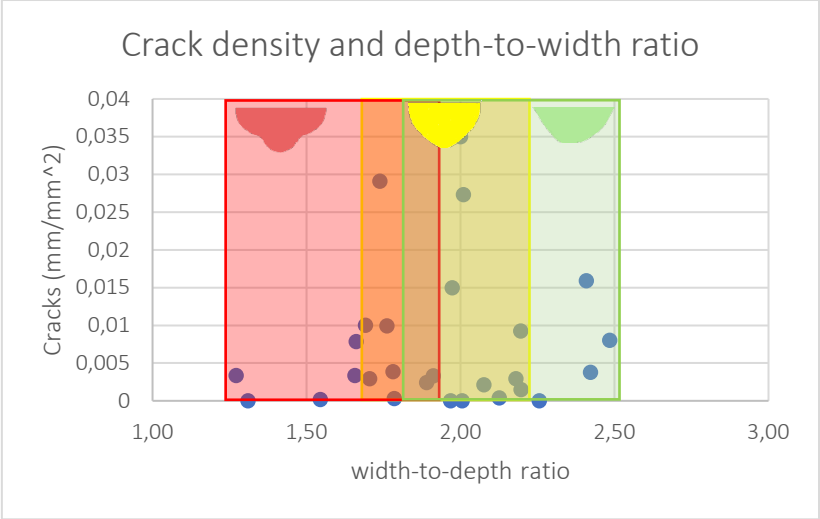

Figure 38. Graph showing the depth-to-width ratio correlation to crack density. There are overlapping between the shapes. Red(Keyholing): 1.2-1.9. Yellow(Vertical ellipse): 1.65-2.2. Green(Horizontal ellpise):1.7-2.4

4.3 Hot isostatic pressing and heat treatment

For chapters about hot isostatic pressing and heat treatment sample numbers referred to corresponds to the samples in Appendix C 5.

4.3.1 Macro cracks and heat treatment

It was found that after HIP substantial macro cracking occurred in samples. Some of the macro crack that formed during HIP stretched all the way down to the centre, as shown in Figure 39.

Figure 39. Macro cracking that occurred after HIP and heat treatment.

To determine the reason for macro cracking and to find an optimal heat treatment cycle, several heat treatments were created and tested as shown in Table 13.

Table 13. Text matrix used for heat treatment with results.

	Temperature (°C)	Heating rate (°C/min)	Dwell time (min)	Cracks
1	600	Slow	120	No
2	700	Slow	120	No
3	100:500:1050:1200	05:05:35:05	30:30:120:FC	Yes
4	400:1050:1200	05:35:05	30:120:FC	Yes
5	100:600:1150:1200	05:05:35:05	30:30:120:FC	Yes
6	Post HIP: 850	Slow	120	Yes
7	600:RT:1200	Slow	60:RT Over night:120:FC	Yes
8	600:RT:1200	Slow	60: RT Over night:120:AC	Yes
9	600:RT:1200	Slow	60: RT Over night:120:Qu	Yes

FC – Furnace Cooling. AC – Air Cooling. Qu – Quench or fast cooling. RT – Room temperature
Slow – uncontrolled heating, roughly 5°C/min

The purpose of heat treatment 7-9 was to test different cooling rates to determine if cracking occurred due to thermal stresses during the cool-down phase. As can be seen in Table 13, the samples in all of these tests suffered from cracking. Below 700°C on the other hand, it was possible to relax the material at 600-700°C for up to 100 minutes without macro-cracking, as shown from heat treatment 1 and 2. This suggests that the ductility drops faster than the material can be relaxed at temperatures above 700 °C, as described in section 2.2.4.4. From the third heat treatment, cracking was observed during heating and thus the cracking mechanism was determined to be strain age cracking. As seen in Figure 10 at 1134 °C the γ’ phase dissolves completely and the highest transformation rate is around 1050°C after which the transformation slows down which is why heat treatment 5 was developed. Heat treatment 6 was developed to try the aging temperature according to ASM guidelines on a HIPed sample.

The result of the heat treatment tests was not entirely conclusive but two different thermal cycle was found for optimal heat treatment in HIP cycles based on the heat treatment trials in Table 13. Even if the heat treatment tests showed a high risk of cracking, an applied pressure, as in HIP, reduces the risk of SAC and enables faster heating rate and thus avoid macro cracking. One of the heating strategies are shown in Figure 40.

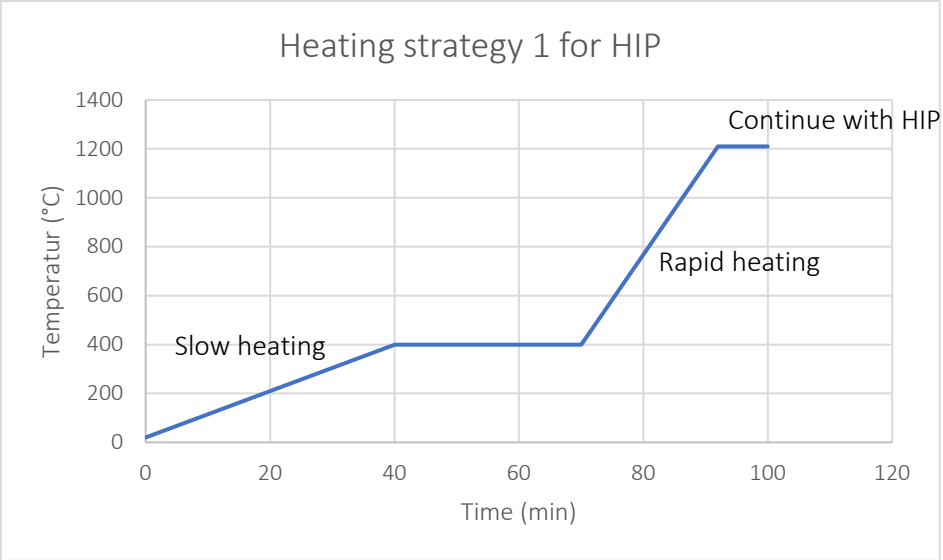

Figure 40. Strategy 1 for heat treatment.

The reason for a dwell time at 400°C in Figure 40 is because Etter et al. [29] found a dip in thermal expansion at 450°C and it is important that the material have a homogenous temperature when the thermal contraction happens. The heating rate should at least be 35°C/min from 400-1200°C. However with this strategy there is still a risk that the thermal contraction that occur at 450°C causes troubles. The second heating strategy avoids the thermal contraction problem with a low heating rate from 400 up to 650°C and offers more relaxtion, heating strategy 2 is shown in Figure 41. A relativly fast heating rate, 20°C/min, is used up to 400 °C to speed up the HIP cycle.

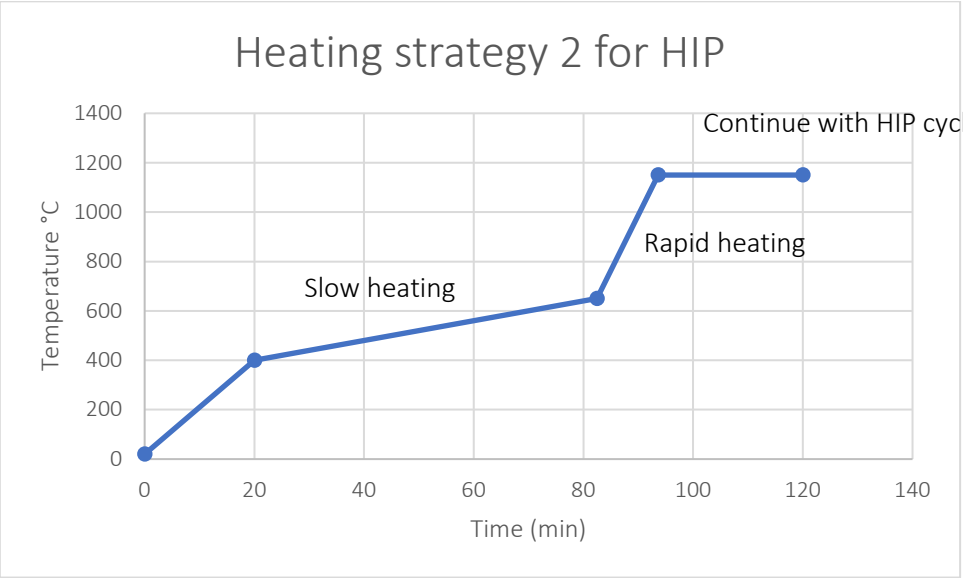

Figure 41. Strategy 2 for heat treatment.

Heating strategy 2 was choosen for the last HIP cycle and with a applied pressure before heating. This apparoach lead to a completely SAC free component that was both HIPed and heat treated successfully.

4.3.2 Defect density

The crack density pre-HIP was measured to 0.14 mm/mm^2. Figure 42 show the average crack density after HIP and HIP + HT with HIP temperature of 1000°C, pressure of 1000 and 2000 bar together with pre-HIP values for comparison. Samples HIPed at 1000°C showed reduction in cracks but complete crack

healing did not take place. A pressure of 2000 bar and temperature of 1210°C during HIP removed cracks which did not reopen after subsequent heat treatment. Application of HIP cycle with 1000°C and a pressure of 1000 bar closed cracks some of which reopened slightly after heat treatment. A temperature of 1000°C and pressure of 1000 bar did not close all cracks with the largest amount of reopening after heat treatment. The crack density is summarized in Appendix B4.

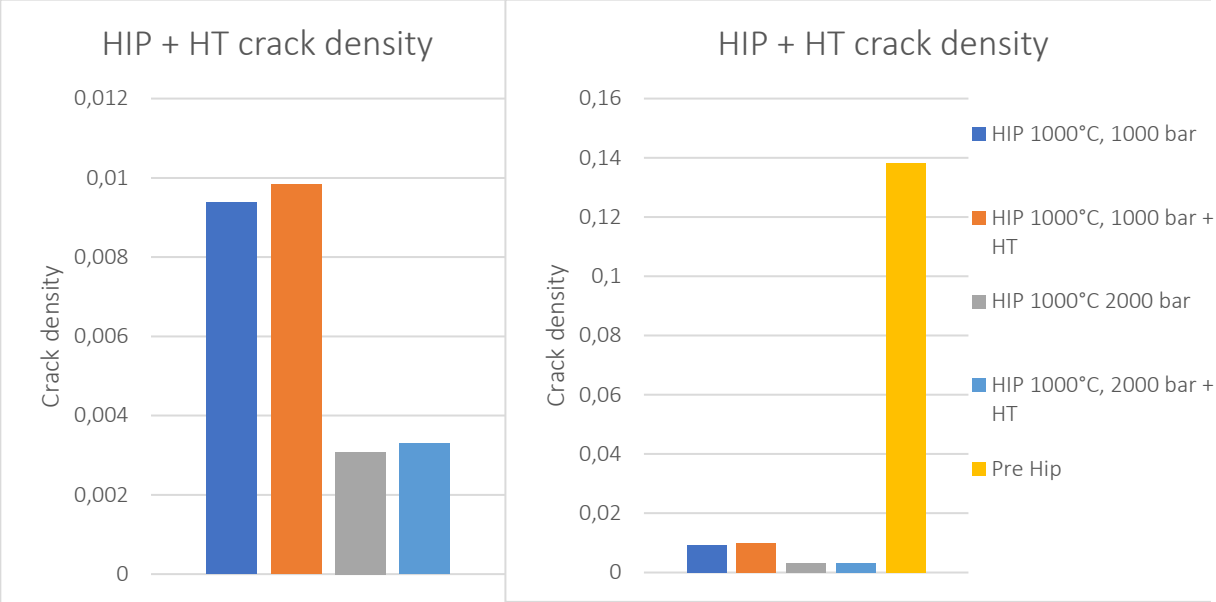

Figure 42. Crack density pre- and post-HIP. Left: Comparison between HIPed samples exposed to different heat treatments. Right: Comparison with pre-HIP levels.

In total, there was a 96% decrease in crack density from pre-Hip to post-Hip at 1000 bar with subsequent heat treatment while HIP without heat treament showed a 98% decrease in crack density. Samples HIPed at 1210° were completely crack free, and thus complete crack healing took place and no crack opening was found with a subsequent heat treatment. Figure 43 shows the resulting total density after HIP and heat treatment compared with pre-HIP density.

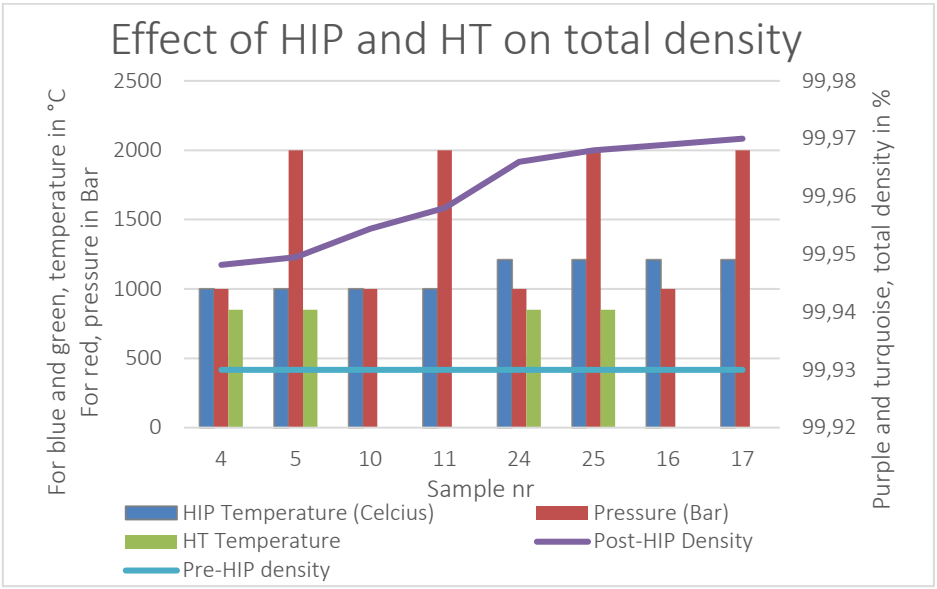

Figure 43. Results from density analysis on HIPed samples with different heat treatment and HIP cycles.

Samples that were HIPed at 1210°C with a pressure of 2000 bars had the highest total density followed by 1210°C with a pressure of 1000 bars. A subsequent heat treatment slightly lowers the total density.

Lowest density was found for the HIP temperature of 1000°C and a pressure of 1000 bars followed by a heat treatment. Figure 44 shows a sample before and after HIP at 1210°C and 200 bar.

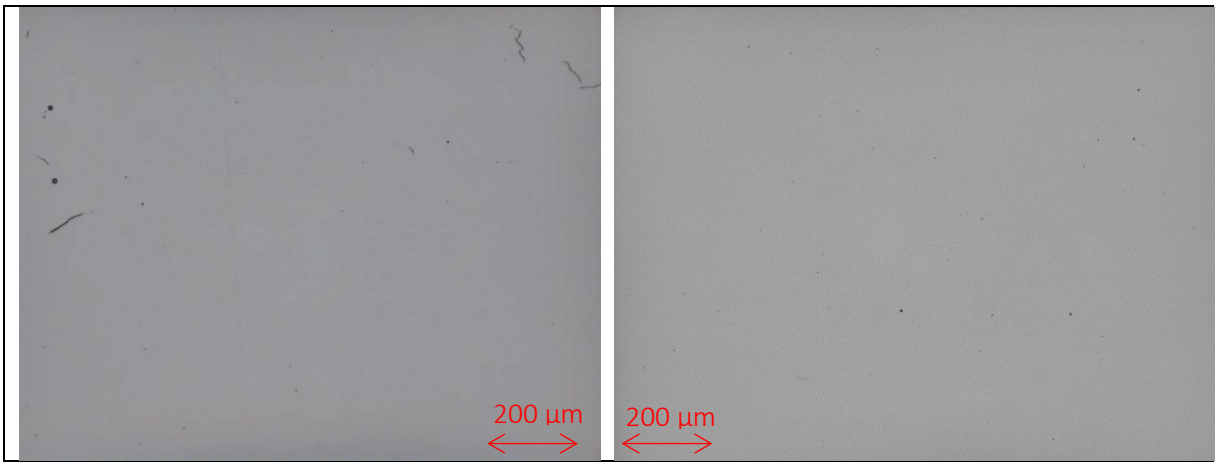

Figure 44. Comparison of pre- and post HIPed sample. Left: As built. Right: HIPed at 1210°C and 2000 bar.

The trend is clear, both for cracks and pore. Higher temperature and higher-pressure results in a crack closure and pore removal. However, a subsequent heat treatment will trigger a regrowth of both cracks and pores, or formation of non-metallic inclusions, but no reopening of completely closed cracks was observed. Pores, if any, present in post-HIP samples at 1210°C and 2000 bar is probably filled with argon gas which regrowth after heat treatment.

4.3.1 Examination of non-metallic inclusions

Selected samples were also analysed by SEM/EDX to examine the pore-like structures remaining after HIP+HT to determine the chemical composition. It was found that all examined areas post-HIP had a chemical composition similar to that of an oxide. Figure 45 shows a typical pore-like structure examined in the SEM/EDX at different magnification. The examined non-metallic inclusions were homogenised spread with a size between 2-10 µm.

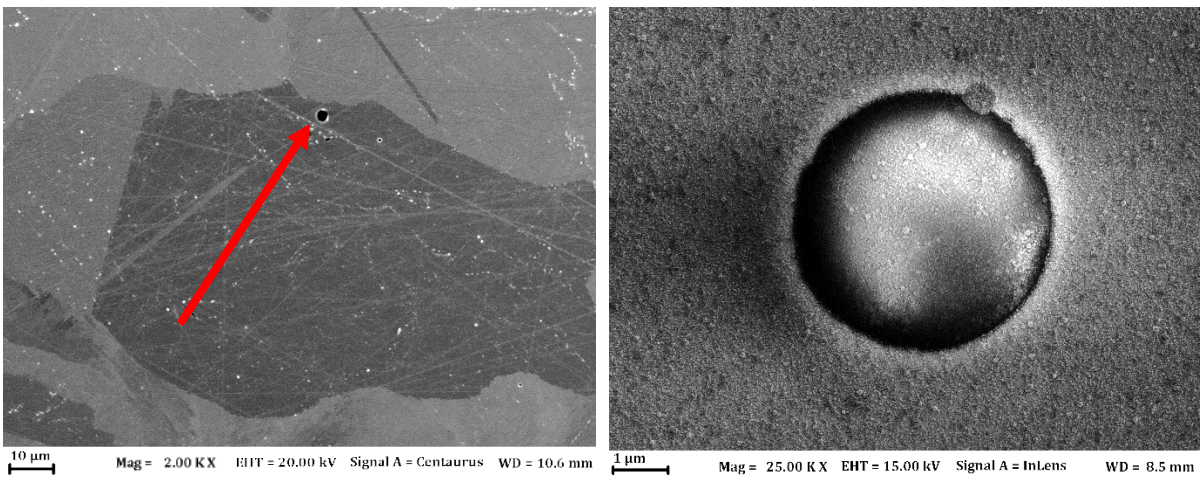

Figure 45. Typical appearance of a pore like structure with the chemical composition of aluminum oxide, HIP temperature of 1210 °C and 1000 bars. The chemical composition is presented in Table 14.

The results from EDX suggests that the pore-like structure in Figure 45 is an aluminum oxide with the chemical composition represented in Table 14. The spectrum location, i.e. the point examined, and the full EDX spectrum is found in Appendix C1 and Appendix C2 respectively. Round pore-like structure was found to usually be aluminum- or titanium-rich oxides.

Table 14. Chemical composition of examined aluminium oxide.

Elements	O	Al	Si	Ti	Cr	Ni	Zr
Wt.%	42.73	44.58	0.71	7.44	1.97	1.25	1.32

Larger and typically non-symmetric, non-metallic, inclusions similar to what is shown in Figure 46 were also examined with a map analysis in EDX. In this case, the result indicated that these types of structures are a silica rich oxide. The mapped area with resulting composition can be found in Appendix C3 and Appendix C4 respectively.

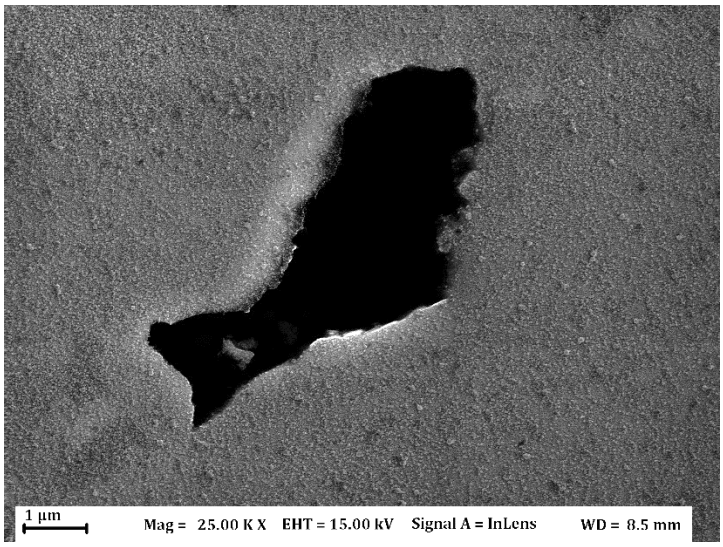

Figure 46. Typical appearance of a pore like structure with the chemical composition of a silica oxide shown in Fig. 45.

Other non-metallic inclusions with varying shapes were examined as well. Nitrides had a symmetric shape with sharp edges and have yellow or gold like color when examined with a light optical microscope. Figure 47 show the three types of non-metallic inclusions found in post-HIP samples.

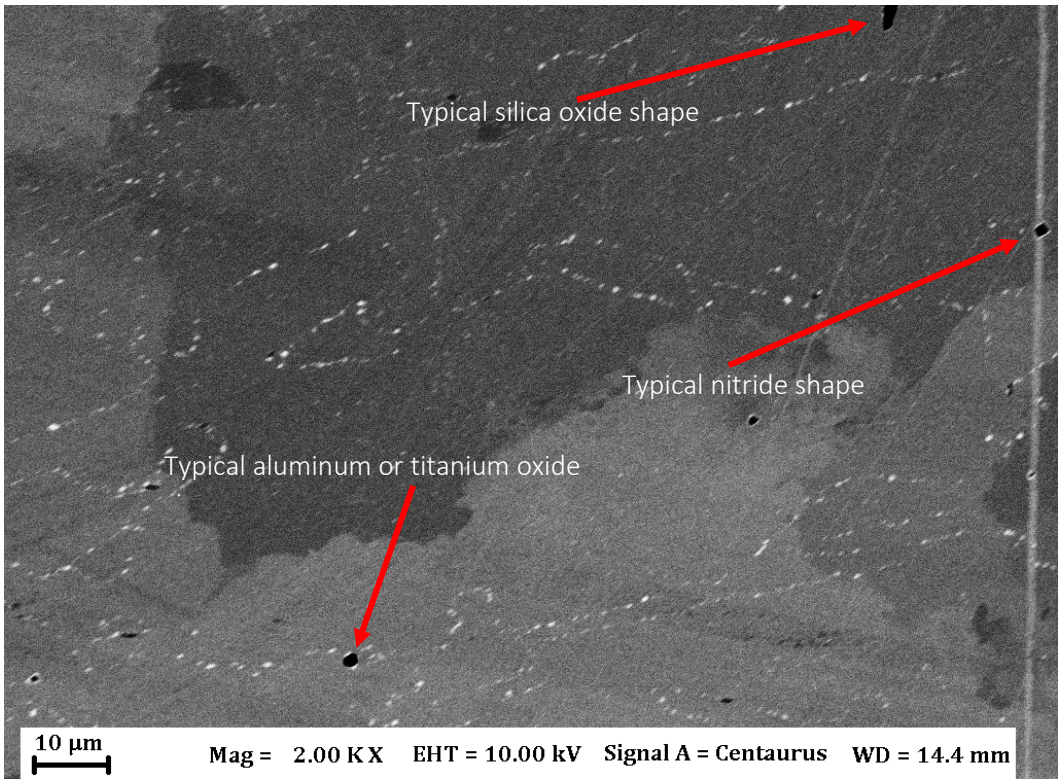

Figure 47. Typical non-metallic inclusions found in post-HIP samples.

The EDX investigation hints that not all defects in post-HIP samples are pores and thus the total density post-HIP is higher than the initial results obtained with light optical microscopy.

4.3.3 Effect on microstructure

As-build grain size is chaotic and anisotropic which makes it hard to measure and the ASTM E112-13 standard cannot be used. A rough estimation for as-built samples is in the range of 5-30 microns in XY-direction with elongated grains in the size range of 50-150 microns in Z-directions. The grain structure of as-built samples is shown in Figure 48.

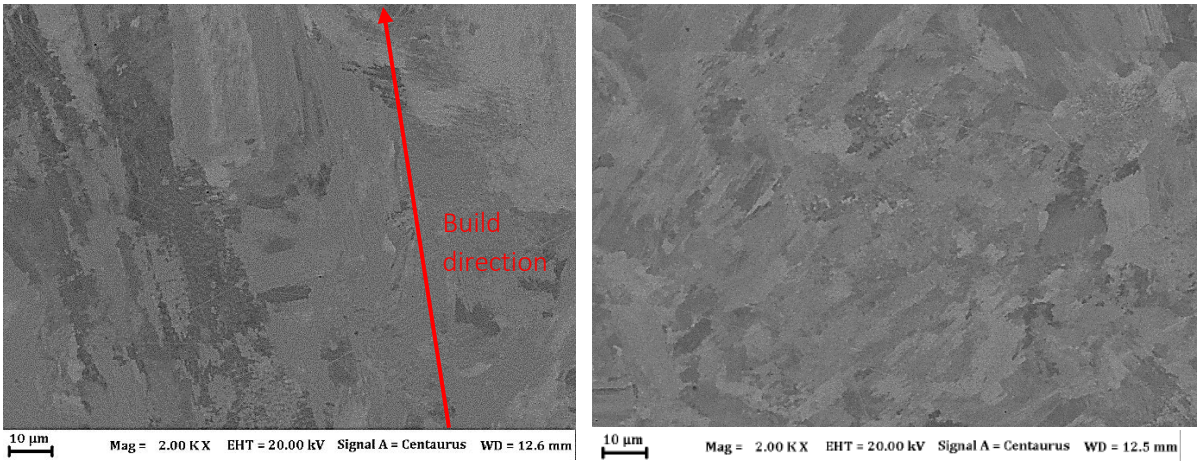

Figure 48. Grains in as-built samples. Left: Z-direction with elongated grains. Right: XY direction with finer grains

The grain size and structure of samples HIPed at 1000 °C showed no change as compared to as-built samples and could therefore not be measured according to any known standard. There was no apparent change in microstructure for 1000 or 2000 bar nor did heat treating induce any change. Figure 49 show

the structure of sample 16, HIPed at 1000 °C and 1000 bars, and sample 26, HIPed at 1000°C and 2000 bars, in XY direction.

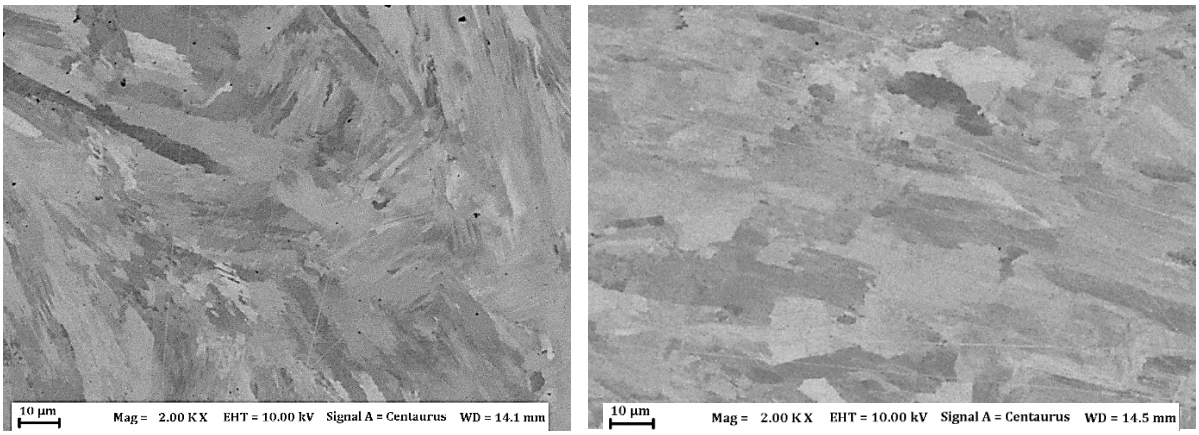

Figure 49. Grain structure of samples HIPed at 1000° and heat treated at 850°C, Z-Direction. Left: Sample 16 HIP pressure at 1000 bar. Right: Sample 24 HIP pressure at 2000 bar.

Samples with a HIP temperature of 1210°C all showed a recrystallized structure. Homogenization occurred in both Z and XY-direction as shown in Figure 50.

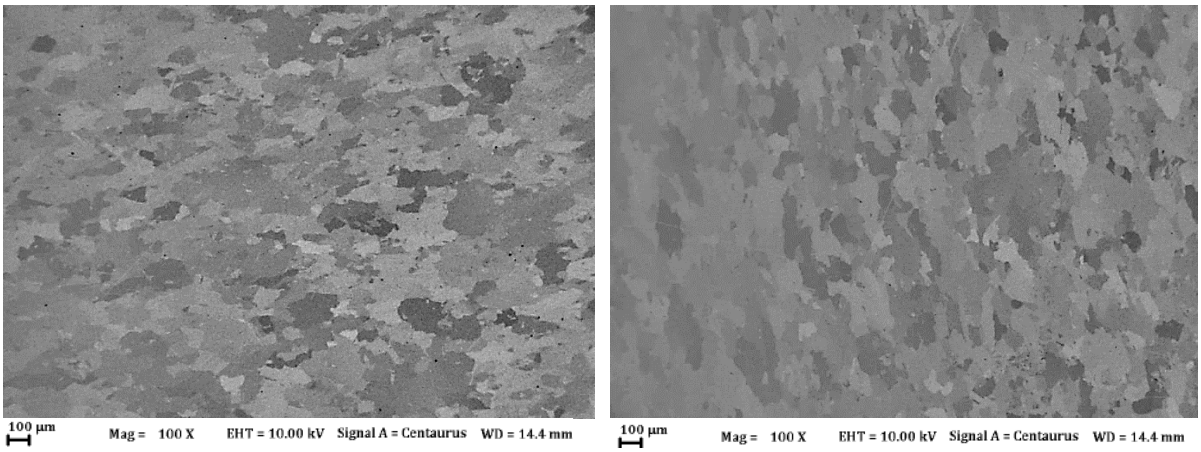

Figure 50. Grain structure HIPed at 1210°C and 2000 bars showing recrystallization, grain growth and homogenization. Left: XY-direction. Right: Z-Direction.

As shown in Figure 50 the grains are not fully equiaxed or homogenous, the reason is that the holding time and temperature were not tailored for controlling grain growth. But there is a clear indication that recrystallization occurs since the chaotic and fine structure from as-build is no longer present. Data from grain measurements are summarized in Table 15 and show that the measured grains are close to the ASTM 112-14 standard meaning that the structure is almost isotropic.

Table 15. Summary of grain measurements and comparison from tables in ASTM E112-4 standard

	Sample 5	Sample 10
Measured grain diameter (µm)	214	196
Measured grain area (mm^2)	0,036	0,029
Measured number grains per mm (No/mm)	5	6
Grain area according to ASTM from measured grain diameter	0,045	0,032
Grains/mm according to ASTM from measured grain diameter	5,26	6,25
HIP temperature (°C)	1210	1210
HIP pressure (bar)	1000	2000
Heat treatment (°C)	850	0

As expected, samples heat treated at 850° had no significant effect on the grain size. However, sample 10 with a HIP pressure of 2000 bar had smaller grains than sample 5 which had a HIP pressure of 1000 bar.

5
Discussion

There is a lot of research done on additive manufacturing of superalloys in recent years about printability of defect free components. There is as time of writing no universal model for optimizing the process for new materials without first performing a set of experiments since each material reacts differently to the process parameters and volumetric energy density. However, the most common approach for optimizing the process parameters seems to be with various variants of design of experiments. It is a relatively fast method to employ when working with new materials. If volumetric energy density is to be used as a standard in the future, a list of parameter coefficient needs to be readily available, and the coefficient are most likely to be obtained empirically from design of experiments.

The material used for this project is a variant of γ' strengthened nickel-base superalloy that has been in development for some time. Traditionally such materials exhibit much higher crack density, sometimes as high as 1 mm/mm^2, which was the reason for the creation of this project. However, this project´s material iteration, showed a remarkable low defect density, especially regarding cracks. The low crack density in the current material lowered the statistical correctness regarding correlations between crack density and process parameters, making the prediction less accurate. This was somewhat compensated by taking more images for the analysis and including all data points from the three designs of experiments in the final analysis. Nonetheless this project showed how robust the current iteration of material is with a low crack density even at the extreme ends of the process window.

Regarding parameters, it seems that laser power and scanning speed are the most influential parameters, regarding crack density, and can compensate each other to a certain degree, i.e. the volumetric energy density theory holds up. Volumetric energy density is also directly connected to the printability of the material. For example, a high laser power that would cause a rough surface can be compensated by an increase in scanning speed. This enables a faster print time which was utilized in DoE 3. There are indications in similar studies that a small hatch distance should be employed to reduce micro cracks. This was not found to be true in this study. Rather, hatch distance shifts the domain where cracks appear in regard to laser power and scanning speed. However, even the highest hatch distance used of 0.06 mm is considered low, whereas earlier works used a hatch distance of 0.1 mm meaning that the assumption that a low hatch distance leads to low crack density cannot be dismissed. Figure 51 show roughly the response found in terms of volumetric energy density and is a good indication on how robust the material is towards cracking.

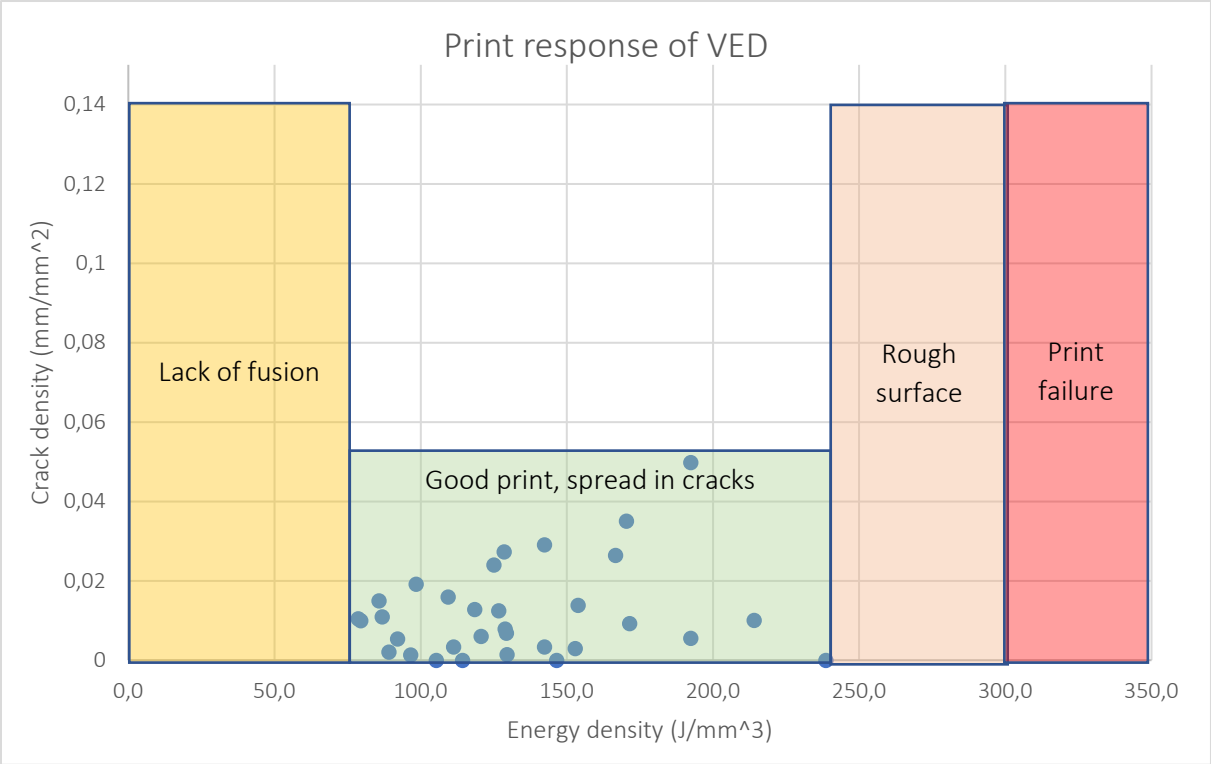

Figure 51. Estimated LPBF response of volumetric energy density values

Melt pool size and shape relates mostly to laser power and scanning speed in the relation of power/speed which gives a good model on the characteristic of melt pools, whereas hatch distance showed low correlation. Unfortunately, no correlation between melt pool geometry and crack density was found in this study. One reason for this could be that the material had such a good resistance to micro-cracking that the effect of melt pool is neglectable. However, it is good praxis to avoid key holing and tailor the energy density, Laser power / scanning speed, below 0.16 J*s/mm to lower the amount of residual stress.

It was assumed that there were two likely reasons for the crack formation during HIP and heat treatment, either due to thermal stress when the material is cooled rapidly or that strain age cracking occurring because the rapid drop in ductility that follows γ’ phase formation. S. Caprioli et al [30] hints that it is possible that transversal thermal cracks can form if there is a defect that can acts as a nucleation point with a present load, and since LPBF materials have a significant amount of residual stress it seems plausible. Strain age cracking is a well-known phenomenon for non-weldable materials and is also a likely reason for macro cracking since the time spent in temperature range 700-1050 °C is enough to fully saturate the material with γ’ precipitates. Due to the sudden drop in ductility from the transformation of γ’ and the existing residual stress or strain is enough to yield the material. Strain age cracking occurs during heating while thermal stress cracking occurs during cooling. The easiest way to determine which mechanism is responsible for the macro cracks is to replicate the thermal cycle used during HIP while observing the sample and see if cracking occurs during heating or cooling. For strain age cracking, residual stress from printing is a major factor, so much that without any residual stress, or strain, there can be no strain age cracking. Cracking due to thermal contraction on the other hand are governed by the cooling rate. However, since the macro cracking was observed during heating it is most likely strain age cracking.

The first HIPed samples cracked due to strain age cracking. The in-house heat treatment that were constructed and tested showed that if the material spent any significant time above 700 °C large crack

appears along the samples. Figure 52 show the TTT diagram for γ' formation which show that it takes less than 1 minute to form 20% γ' at temperatures above ~900 °C.

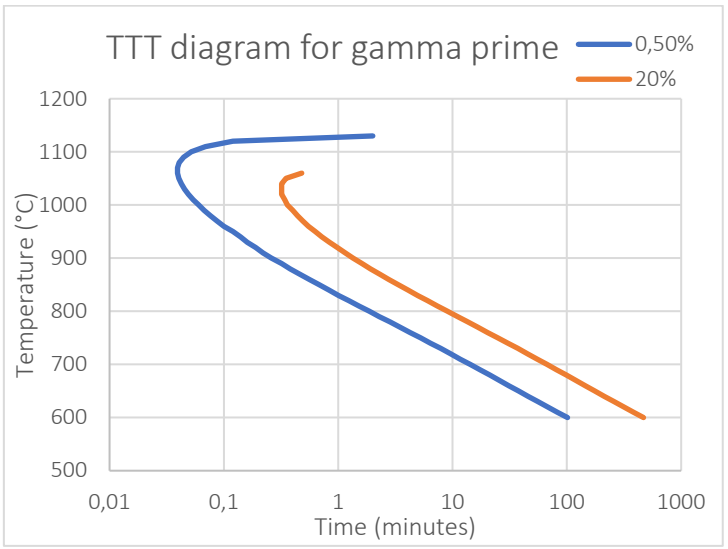

Figure 52. TTT diagram for the current material showing the transformation of the gamma prime phase.

The relaxation process, which removes residual stress in a material, is performed at elevated temperature and for non-weldable materials this temperature is within the aging range and the material will loss ductility much faster than it is relaxed. The paradox is that the material needs to be relaxed, but to relax it the temperature required forms γ' and cracks if the material is not relaxed prior. With simulations and literature review, different heat treatment cycles were created and tested and the results showed significantly smaller cracks with a tailored heat treatment compared to what formed with uncontrolled parameters, however all samples showed some cracking. One reason for smaller cracks with the tailored heat treatment could be that the material has time to relax somewhat before it loses ductility. The final solution stems from the fact that compressive stress will hinder or at least slow down crack formation and phase transformation. Thus, increased pressure during HIP before starting the heat treatment was implemented and showed good success. None of the HIPed sample that used the formulated heat strategy cracked. Since it is not clear if full relaxation takes place during the densification process, it is recommended to apply pressure during the subsequent heat treatment as well. Regarding the heat treatment tests, according to patent US 2015/0322557 A1 [29] the critical temperature range is 400-1050°C which is the reason for a dwell time at 1050°C before solutionizing at 1200° for sample 3 and 4. Since sample 3 and 4 cracked, test run 5-9 was formed with help of simulation from JMatPro, by simulating when γ' starts forming and at which rate, the heat treatment cycles was tailored to avoid the critical temperature range and dwell time.

The microstructure of as-built samples showed a non-homogenous elongated grain in the build direction, as expected. Recrystallisation did not occur at 1000 °C which is just above the service temperature of the material. There was no visible change to the structure for HIP at 1000°C with a subsequent heat treatment at 850°C. This indicates that a full annealing process is required to be able to tailor the material. After HIP at 1210 °C recrystallization and homogenization occurred in both XY and Z direction, however the effect of pressure was negligible on shape, size and distribution of the grains.

HIP is a process that fit very well in enabling the freedom of design that additive manufacturing gives. It enables a higher total density as well as cracks to be present in as built material since there is a considerable densification process and HIP is shown to close cracks. S. Tammas-Williams et al [22] found that defects closed by HIP can regrow during heat treatment in additivly manufactured titanium

components. The reason for this is that argon is not soluble in titanium and thus wont diffuse to the surface but rather be compressed when the pores shrinks. After a subsequent heat treatment the argon will expand at the same time as the materials flowstress is lowered and thus the pores can open up again. Similar responses are found for nickel-base superalloys where HIP without heat treatment give the highest density while a subsequent heat treatment lower the total density slightly. Even with a subsequent heat treatment, where some defects seemed to open again, the resulting density after HIP is close to 100%. Added to this is the ability to heat treat a material under pressure which was found to be a necessity for this material if strain age cracking is to be avoided. The EDX analysis of the non-metallic inclusions indicates that a lot of the pore-like structure are more likely to be some kind of oxide or nitride in samples HIPed at 1210 °C.

Several times during printing the support structure caused a print failure which lead to a lot of delays. More time should have been assigned to researching and tailoring the support structure to avoid these delays. In total there were 6 samples that were aborted during print, if possible they were examined for cracks and if not, they were used to screen out areas to avoid. There are also some procedures that might have needed more consideration such as if removal from build plate affects the samples, if a heated build plate should be used etc. Furthermore, the scan pattern should have been considered as a tool to reduce residual stress. Scan pattern is the path a laser beam covers when melting a cross section area. By applying a scanning strategy, residual stresses in the material that form due to thermal cycles and large temperature gradients can be lowered. By optimizing the scan pattern it is possible to lower the residual stresses at a macroscale since there will be no preferred direction for distortion, the stress is averaged out in all directions [3].

6
Conclusion

Nickel-base superalloys can be produced using LPBF with a full density and low crack density. From the design of experiments, it is concluded that the volumetric energy density theory is an overall viable approach to control build quality, even though a direct correlation to crack density was not found. Furthermore, there were no indication that melt pool characteristics played any role in the formation of cracks in the investigated range of process parameters. Nevertheless, it is possible to control melt pools and thus avoid keyholing.

Hot isostatic pressing is shown to greatly reduce cracks and pores in the material. For densification, temperature is the main parameter and it is recommended that HIP should be performed above the γ' solvus temperature which, based on simulations, is around 1137°C. There were indications that pores regrow during heat treatment while cracks did not. The reason for this is probably trapped argon gas in the pores that are not present in cracks. When temperatures above the solutionizing temperature were used during HIP, recrystallization took place and the material was homogenized.

The optimization process aside, the main conclusion is that even highly stressed non-weldable superalloys can be heat treated without strain age cracking. This requires an initial stress relieving at low temperature followed by a sufficient heat rate to the solutionizing temperature together with an external pressure offered in the HIP cycle. This makes HIP the ideal solution for obtaining crack free LPBF parts from precipitation strengthened superalloys

7
Future recommendations

Most of the samples produced for the optimisation study had a simple geometry. In order to ensure good print quality, it is recommended to do one more design of experiment on more complex parts. Furthermore, before these parameters are to be used for larger, complex and useable components, there are some settings in the machine that needs to be examined, for example *up*- and *down*-skin as well as the outer most layer called *skin*. The parameter experimented on in this thesis is only for the bulk component, called *core*.

It is also recommended that the formulated heat treatment is tested on more complex components to find out if more tailoring is required. There are standards on how to heat treat γ' strengthened super alloys to control the grain growth which should be tested more thoroughly under pressure to ensure good results. A measurement of γ' is also recommended after heat treatment followed by strength and creep test to ensure that the LPBF + post process yields the desired strength.

Furthermore, an examination on the non-metallic inclusions with TEM or AES is recommended to understand the origin and formation of oxides during LPBF processing.

References

[1] C. T. Sims, N. S. Stoloff, and W. C. Hagel, “Superalloys II,” in *Superalloys II*, 1987, p. 615.

[2] S. Suresh, *Fatigue of Materials*. Cambridge University Press, 1998.

[3] I. Gibson, D. W. Rosen, and B. Stucker, *Additive manufacturing technologies: Rapid prototyping to direct digital manufacturing*. 2010.

[4] H. Atkinson and S. Davies, “Fundamental aspects of hot isostatic pressing: an overview,” *Metall. Mater. Trans. A*, vol. 31A, no. December, pp. 2981–3000, 2000.

[5] B. Geddes, H. Leon, and X. Huang, *Superalloys: Alloying and Performance*. Cleveland: ASM International, 2010.

[6] D. Porter, K. Easterling, and S. Mohamed, *Phase Transformations in Metals and Alloys*, Third. Miami: CRC Press, 2008.

[7] a Lingenfelter, “Welding of Inconel Alloy 718: A Historical Overview,” *Superalloys 718 Metall. Appl.*, pp. 673–683, 1989.

[8] X. Wu, “A review of laser fabrication of metallic engineering components and of materials,” *Mater. Sci. Technol.*, vol. 23, no. 6, pp. 631–640, 2007.

[9] K. Kunze, T. Etter, J. Grässlin, and V. Shklover, “Texture, anisotropy in microstructure and mechanical properties of IN738LC alloy processed by selective laser melting (SLM),” *Mater. Sci. Eng. A*, vol. 620, pp. 213–222, 2014.

[10] D. Gu, *Laser additive manufacturing of high-performance materials*. 2015.

[11] L. N. Carter, K. Essa, and M. M. Attallah, “Optimisation of selective laser melting for a high temperature Ni-superalloy,” *Rapid Prototyp. J.*, vol. 21, no. 4, pp. 423–432, 2015.

[12] M. Cloots, P. J. Uggowitzer, and K. Wegener, “Investigations on the microstructure and crack formation of IN738LC samples processed by selective laser melting using Gaussian and doughnut profiles,” *Mater. Des.*, vol. 89, no. October 2015, pp. 770–784, 2016.

[13] X. Zhao, X. Lin, J. Chen, L. Xue, and W. Huang, “The effect of hot isostatic pressing on crack healing, microstructure, mechanical properties of Rene88DT superalloy prepared by laser solid forming,” *Mater. Sci. Eng. A*, vol. 504, no. 1–2, pp. 129–134, 2009.

[14] L. E. Murr *et al.*, “Metal Fabrication by Additive Manufacturing Using Laser and Electron Beam Melting Technologies,” *Journal of Materials Science and Technology*, vol. 28, no. 1. pp. 1–14, 2012.

[15] O. A. Ojo and N. L. Richards, “Heat-affected zone cracking in welded nickel superalloys,” in *Welding and Joining of Aerospace Materials*, 2011, pp. 142–177.

[16] L. N. Carter, M. M. Attallah, and R. C. Reed, “Laser Powder Bed Fabrication of Nickel-Base Superalloys: Influence of Parameters; Characterisation, Quantification and Mitigation of Cracking,” in *Superalloys 2012*, 2012, pp. 577–586.

[17] S. Kou, “Solidification and liquation cracking issues in welding,” *Jom*, vol. 55, no. 6, pp. 37–42, 2003.

[18] H. S. Yang and B. C. Lee, “A Study on the Effect of Gap Width on Residual Stresses of LaserWelded Dissimilar Joints,” vol. 326–328, no. January, pp. 669–672, 2017.

[19] ASM International, *ASM Handbook Volume 04 - Heat Treating*. 1991.

[20] M. Lamberigts, E. Diderrich, and D. Coutsouradis, “Hip’ing various precision cast engine components in nickel-base superalloys,” *Superalloys 1980*.

[21] S. Tammas-Williams, P. J. Withers, I. Todd, and P. B. Prangnell, “The Effectiveness of Hot Isostatic Pressing for Closing Porosity in Titanium Parts Manufactured by Selective Electron Beam Melting,” *Metall. Mater. Trans. A Phys. Metall. Mater. Sci.*, vol. 47, no. 5, pp. 1939–1946, 2016.

[22] S. Tammas-Williams, P. J. Withers, I. Todd, and P. B. Prangnell, “Porosity regrowth during heat treatment of hot isostatically pressed additively manufactured titanium components,” *Scr. Mater.*, vol. 122, pp. 72–76, 2016.

[23] J. Antony, *Design of Experiments for Engineers and Scientists*, no. October. 2003.

[24] Y. Dodge, *The concise encyclopedia of statistics*. Springer, 2002.

[25] J. Goupy and L. Creighton, *Introduction to Design of Experiments, With JMP Examples*. Cary: SAS, 2008.

[26] A. I. Khuri and S. Mukhopadhyay, “Response surface methodology,” *Wiley Interdiscip. Rev. Comput. Stat.*, vol. 2, no. 2, pp. 128–149, 2010.

[27] EOS, “EOS m290.” [Online]. Available: https://www.eos.info/eos-m290. [Accessed: 25-Apr-2018].

[28] N. Perevoshchikova *et al.*, “Optimisation of selective laser melting parameters for the Ni-based superalloy IN-738 LC using Doehlert’s design,” *Rapid Prototyp. J.*, vol. 23, no. 5, pp. 881–892, 2017.

[29] O. F. Ac and P. For, “(12) Patent Application Publication (10) Pub. No.: US 2017/0139001 A1,” vol. 1, no. 19, 2017.

[30] S. Caprioli, T. Vernersson, and A. Ekberg, “Thermal cracking of a railway wheel tread due to tread braking-critical crack sizes and in fluence of repeated thermal cycles,” *Proc. Inst. Mech. Eng. Part F J. Rail Rapid Transit*, vol. 227, no. 1, pp. 10–18, 2013.

[31] Wikimedia Commons contributors, "File:Keyhole welding scheme.png," *Wikimedia Commons, the free media repository*, https://commons.wikimedia.org/w/index.php?title=File:Keyhole_welding_scheme.png&oldid=138949315(accessed June 10, 2018).

A
Appendix

Sample #	Power (W)	Hatch distance (mm)	Scanning speed (mm/s)	Energy density (J/mm³)	Comment
1	100	0,04	1000	125,0	Failed print
2	100	0,05	1300	76,9	LOF
3	100	0,06	1600	52,1	LOF
4	200	0,04	1300	192,3	OK
5	200	0,05	1600	125,0	OK
6	200	0,06	1000	166,7	OK
7	300	0,04	1600	234,4	Failed print
8	300	0,05	1000	300,0	Failed print
9	300	0,06	1300	192,3	OK
10	200	0,05	1300	153,8	OK

Appendix A:1 Design of experiment 1 design matrix

Sample #	Total crack area (um)	% Cracks	cracks (mm/mm^2)	Total pore area (um)	% Pore	Total density
1						
2						
3						
4	21,124	0,00083621	0,005538446	269,853	0,074776	99,92439
5	101,455	0,00401617	0,024032524	725,946	0,20116	99,79482
6	118,711	0,00469927	0,026392628	836,926	0,231913	99,76339
7						
8						
9	602,139	0,02383614	0,089827297	431,569	0,119588	99,85658
10	57,007	0,00225667	0,01381979	362,421	0,100427	99,89732

Appendix A:2 Design of experiment 1 results from defect analysis

Sample #	Power (W)	Hatch distance (mm)	Scanning speed (mm/s)	Energy density (J/mm³)	Comment
1	225	0,05	1750	128,57143	OK
2	300	0,05	1750	171,42857	Rough surface to high power
3	262,5	0,05	2399,5	109,39779	Ok
4	187,5	0,05	2399,5	78,141279	Lack of fusion
5	150	0,05	1750	85,714286	OK
6	187,5	0,05	1100,5	170,3771	Failed print
7	262,5	0,05	1100,5	238,52794	Failed print
8	262,5	0,06	1966,75	111,2241	Ok

9	187,5	0,06	1966,75	79,445786	Ok
10	225	0,06	1317,25	142,342	Ok
11	262,5	0,04	1533,25	214,0062	Rough surface to high power
12	187,5	0,04	1533,25	152,86157	Rough surface to high power
13	225	0,04	2182,75	128,85122	Ok
14	150	0,04	1317,25	142,342	Ok

Appendix A: 3 Design of experiment 2 design matrix

Sample #	Total crack area (µm)	% Cracks	cracks (mm/mm^2)	% Pore	Total density	Defect density
1	958,259	0,007419	0,027326043	0,377581339	99,95722222	0,042777778
2	218,113	0,0019	0,00924056	0,349100336	99,956125	0,043875
3	770,281	0,006709	0,015929921	0,215291208	99,97225	0,02775
4	7776,848	0,067733	0,130124519	1,805267239	99,765875	0,234125
5	271,493	0,003153	0,015001542	0,438847228	99,92633333	0,073666667
6	1645,6	0,009555	0,035018559	0,824445055	99,9305	0,0695
7	0	0	0	0,054	99,991	0,009
8	81,219	0,000943	0,003381856	0,099056827	99,98333333	0,016666667
9	360,46	0,003588	0,009955053	0,243412068	99,96471429	0,035285714
10	43,336	0,000604	0,003347947	0,105396101	99,9788	0,0212
11	205,198	0,002042	0,010021743	0,193957509	99,972	0,028
12	46,205	0,000644	0,002961801	0,121356121	99,9756	0,0244
13	158,992	0,001385	0,007856962	0,283615253	99,964375	0,035625
14	813,33	0,007084	0,029123218	0,279916271	99,964125	0,035875

Appendix A:4 Design of experiment 2 results from defect analysis

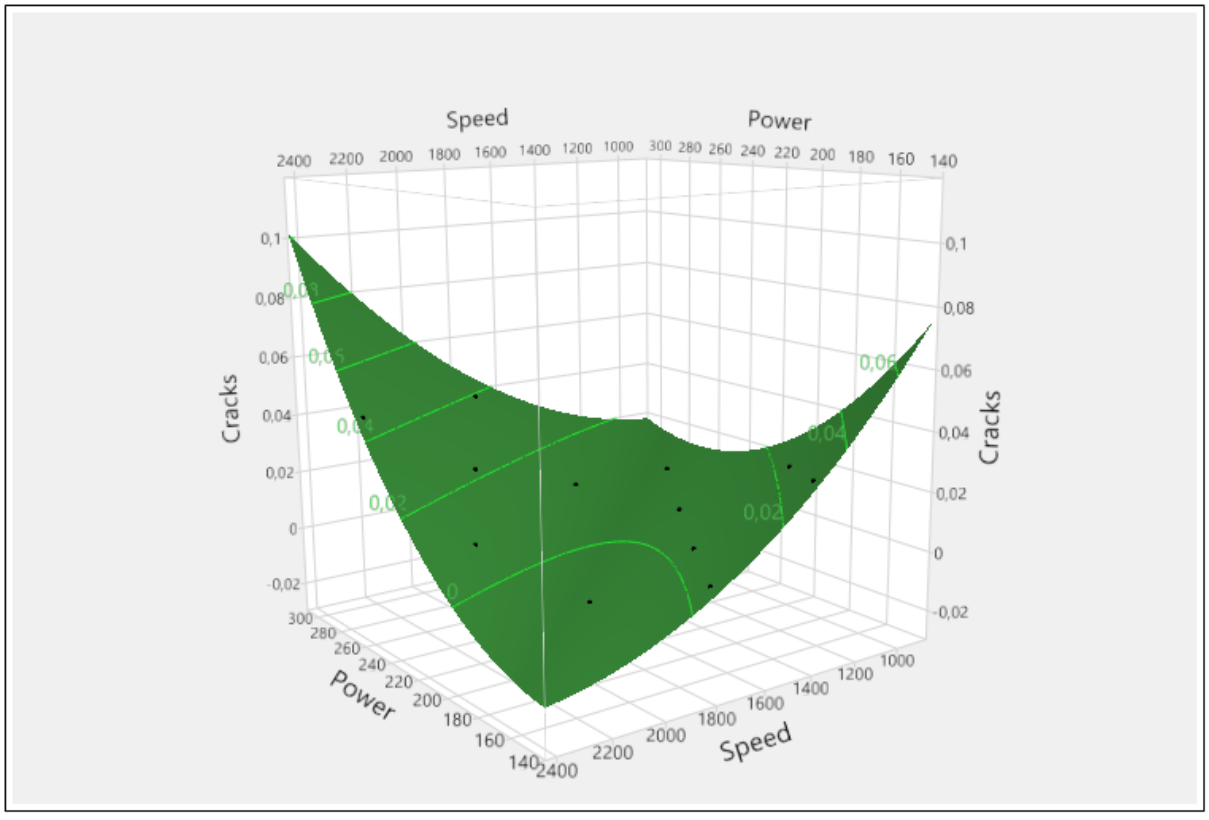

Appendix A:5 Entire surface plot for design of experiment 2.

Sample #	Power (W)	Hatch distance (mm)	Scanning speed (mm/s)	Energy density (J/mm³)
1	200	0,05	1900	105,2632
2	225	0,05	1900	118,4211
3	212,5	0,05	2159,8	98,38874
4	187,5	0,05	2159,8	86,81359
5	175	0,05	1900	92,10526
6	187,5	0,05	1640,2	114,3153
7	212,5	0,05	1640,2	129,5574
8	212,5	0,06	1986,7	89,13441
9	187,5	0,06	1986,7	78,64801
10	200	0,06	1726,9	96,51205
11	212,5	0,04	1813,3	146,4871
12	187,5	0,04	1813,3	129,2533
13	200	0,04	2073,1	120,5923
14	175	0,04	1726,9	126,6721

Appendix A: 6 Design of experiment 3 design matrix

Sample #	Total crack area (µm)	% Cracks		cracks (mm/mm^2)	% Pore	Total density %	Defect density %
1		0	0	0	0,358	99,9642	0,0358
2		558,97	0,003895	0,003895	1,079105	99,8917	0,1083
3		919,972	0,008013	0,008013	0,310987	99,9601	0,039875
4		656,208	0,00381	0,00381	0,59019	99,9505	0,0495
5		214,854	0,001497	0,001497	0,284503	99,9714	0,0286
6		0	0	0	0,111	99,9889	0,0111
7		23,291	0,00018	0,00018	0,21282	99,9763	0,023667
8		66,378	0,000385	0,000385	0,403615	99,9663	0,033667
9		508,606	0,002953	0,002953	0,671047	99,9438	0,056167
10		47,163	0,000299	0,000299	0,331701	99,9698	0,030182
11		0	0	0	0,212	99,9807	0,019273
12		347,61	0,002422	0,002422	0,376578	99,9621	0,0379
13		303,939	0,002118	0,002118	0,390882	99,9607	0,0393
14		426,797	0,003304	0,003304	0,462696	99,9482	0,051778

Appendix A:7 Design of experiment 3 results from defect analysis

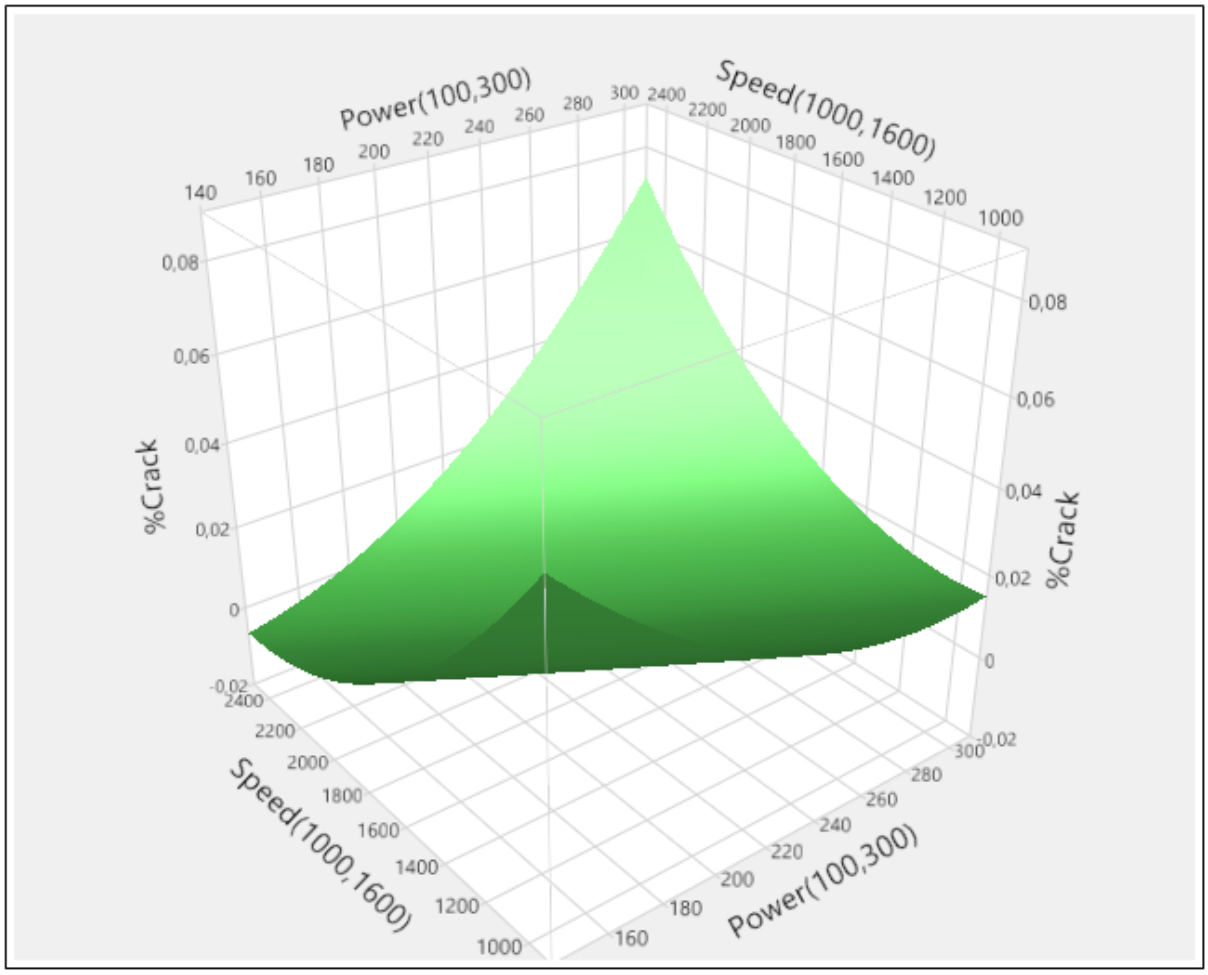

Appendix A:8. 3D response surface from main analysis.

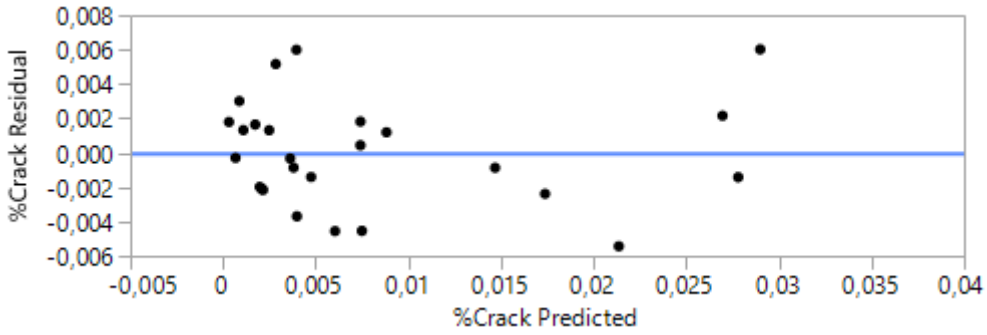

Appendix A:9. Residual by predicted plot

Term	Estimate (Coefficients)	Std Error	t Ratio	Prob>|t|
Intercept	0,0128996	0,003296	3,91	0,0016*
Power(100,300)	-0,019827	0,005146	-3,85	0,0018*
Hd[0,05-0,04]	0,0028233	0,003833	0,74	0,4735
Hd[0,06-0,05]	-0,002445	0,003097	-0,79	0,4430
Speed(1000,1600)	-0,011029	0,002603	-4,24	0,0008*
Power*Power	0,0210014	0,00612	3,43	0,0041*
Power*Hd[0,05-0,04]	-0,018512	0,005877	-3,15	0,0071*
Power*Hd[0,06-0,05]	-0,006408	0,007033	-0,91	0,3776

Term	Estimate (Coefficients)	Std Error	t Ratio	Prob>|t|
Power*Speed	0,0140375	0,002526	5,56	<,0001*
Hd[0,05-0,04]*Speed	-0,000894	0,002046	-0,44	0,6689
Hd[0,06-0,05]*Speed	0,0018435	0,001613	1,14	0,2723
Speed*Speed	0,0024294	0,000694	3,50	0,0035*

Appendix A:10. Response surface coefficient

B
Appendix

Sample nr	Half Melt Pool Width	Melt Pool Depth	Width:Depth radio
1	81,7	81,3	2,010
2	137,9	125,6	2,196
3	81	67,9	2,386
4	54,8	51,2	2,141
5	57,3	58,1	1,972
6	128,1	128,2	1,998
7	120,4	183,8	1,310
8	90,4	109,1	1,657
9	49,6	56,4	1,759
10	72,8	114,4	1,273
11	127,8	151,2	1,690
12	73,9	86,8	1,703
13	61,7	74,2	1,663
14	57,1	65,7	1,738

Appendix B1: Measured melt pool characteristics

Sample nr	Power/speed (W*s/mm)	Melt pool depth (µm)	Geometry
1	0,128571429	81,3	”Deep”. Vertical ellipse
2	0,171428571	125,6	”Deep”. Vertical ellipse
3	0,109397791	67,9	”Shallow”. Horizontal ellipse
4	0,078141279	51,2	”Shallow”. Horizontal ellipse
5	0,085714286	58,1	”Shallow”. Horizontal ellipse
6	0,170377101	128,2	Keyholing
7	0,238527942	183,8	Keyholing
8	0,133468921	109,1	”Shallow”. Horizontal ellipse
9	0,095334943	56,4	”Shallow”. Horizontal ellipse
10	0,1708104	114,4	Keyholing
11	0,171204957	151,2	Keyholing
12	0,122289255	86,8	”Deep”. Vertical ellipse
13	0,103080976	74,2	”Deep”. Vertical ellipse
14	0,1138736	65,7	”Shallow”. Horizontal ellipse

Appendix B2. Correlation between Power/speed and melt pool characteristics

Sample nr	Mean depth (µm)	Width:depth ratio	Predicted melt Pool Depth (µm)	Predicted width:depth ratio	Prediction error depth	Prediction error Width:Depth ratio
1	65,06	2,26	70,79	1,92	8%	18%
2	74,68	1,78	82,26	1,87	9%	5%
3	62,51	2,48	64,79	1,94	4%	28%
4	52,50	2,42	54,70	1,98	4%	22%
5	61,85	2,20	59,32	1,96	4%	12%
6	72,65	2,01	78,68	1,89	8%	6%
7	89,28	1,54	91,97	1,83	3%	16%
8	65,60	2,13	72,27	1,91	9%	11%
9	62,75	2,18	61,30	1,96	2%	11%
10	76,49	1,78	79,99	1,88	4%	5%
11	71,16	1,97	81,19	1,88	12%	5%
12	73,63	1,89	69,17	1,92	6%	2%
13	61,90	2,08	63,13	1,95	2%	7%
14	61,14	1,91	67,37	1,93	9%	1%

Appendix B3. Melt pool data for design of experiment 3 with prediction and accuracy.

Sample nr	Temperature (Celsius)	Pressure (bar)	HT Temp	cracks (mm/mm^2)
4	1210	1000	850	0
5	1210	1000	0	0
10	1210	2000	0	0
11	1210	2000	850	0
16	1000	1000	0	0,0093
17	1000	1000	850	0,014
24	1000	2000	0	0,00328
25	1000	2000	850	0,0033

Appendix B4. Crack density post-hip

C
Appendix

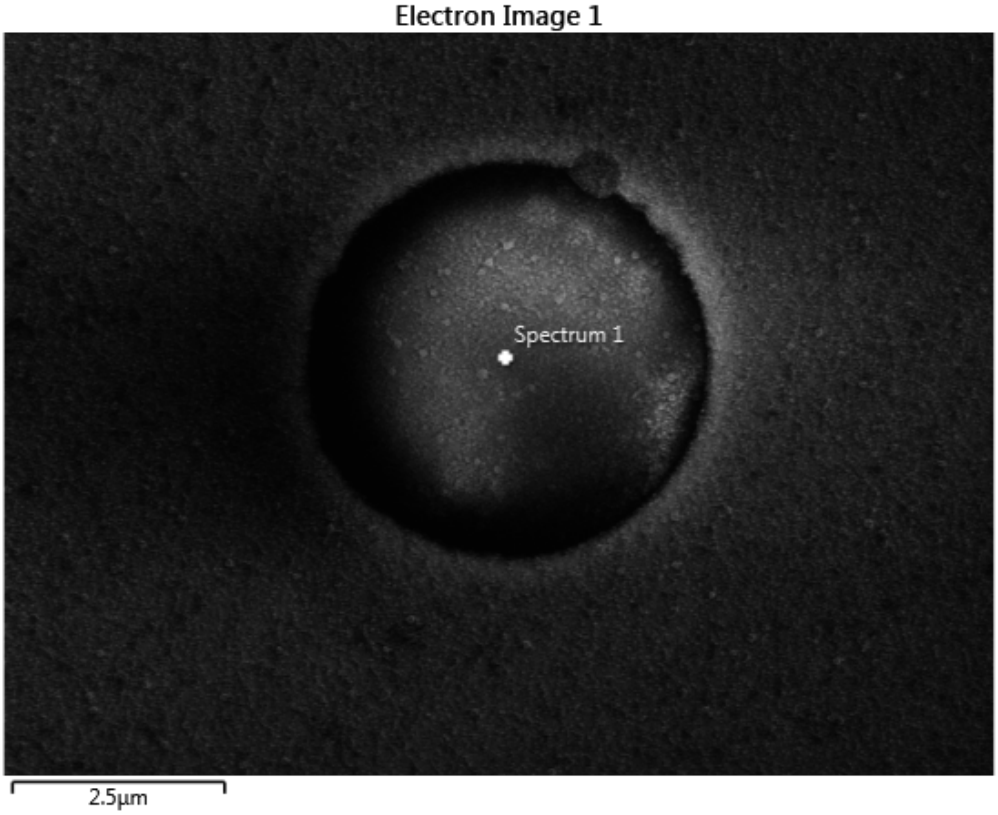

Appendix C1. Spectrum point location.

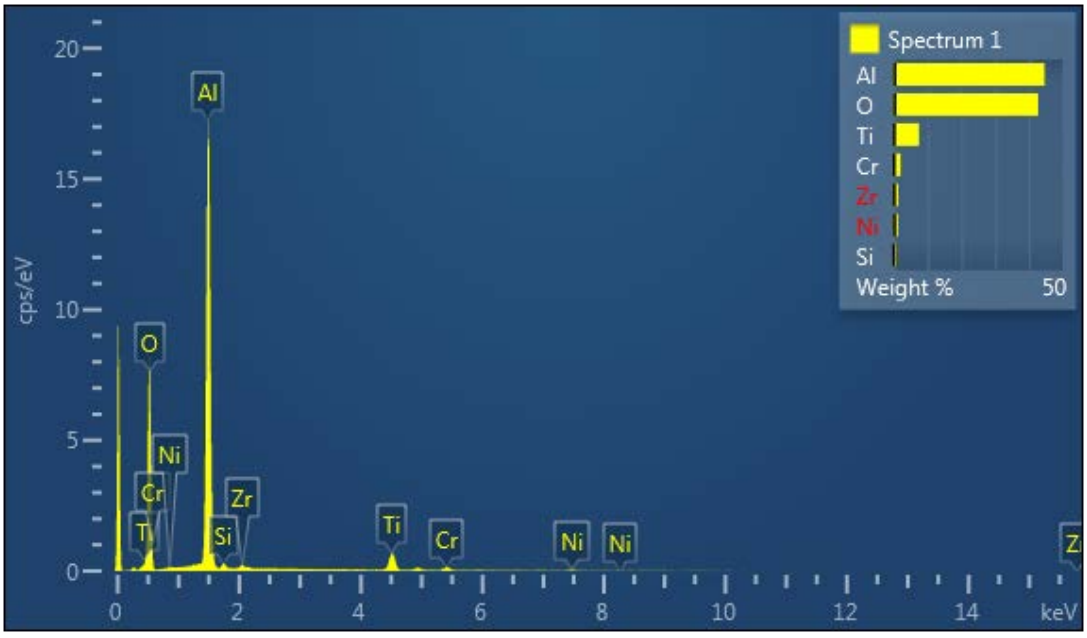

Appendix C2. Resulting composition from Spectrum 1 by EDX

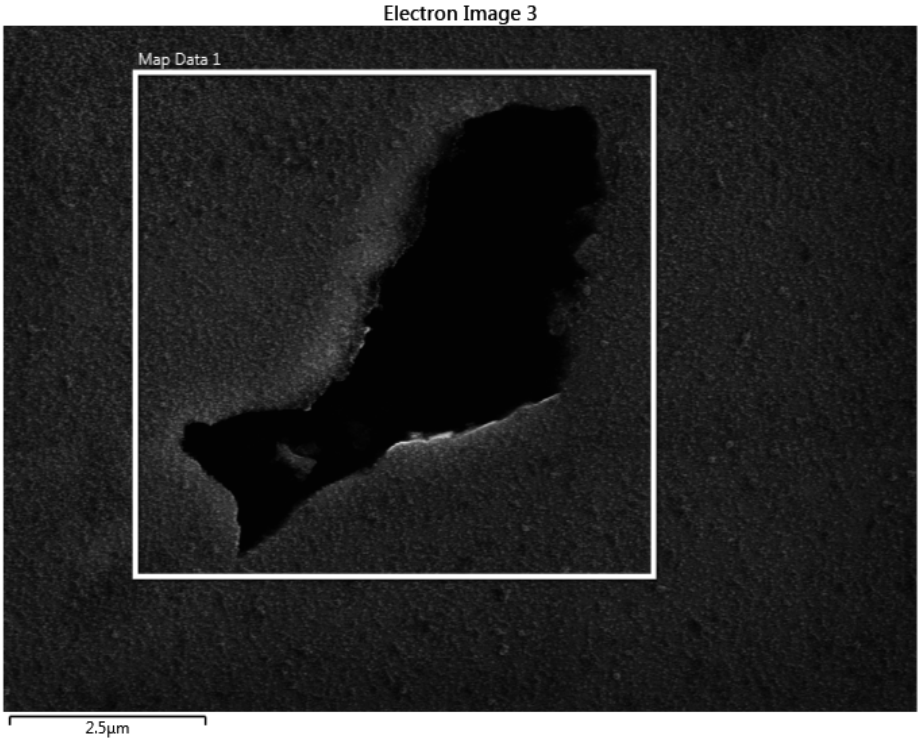

Appendix C3. Map data or examined area of the silica oxide

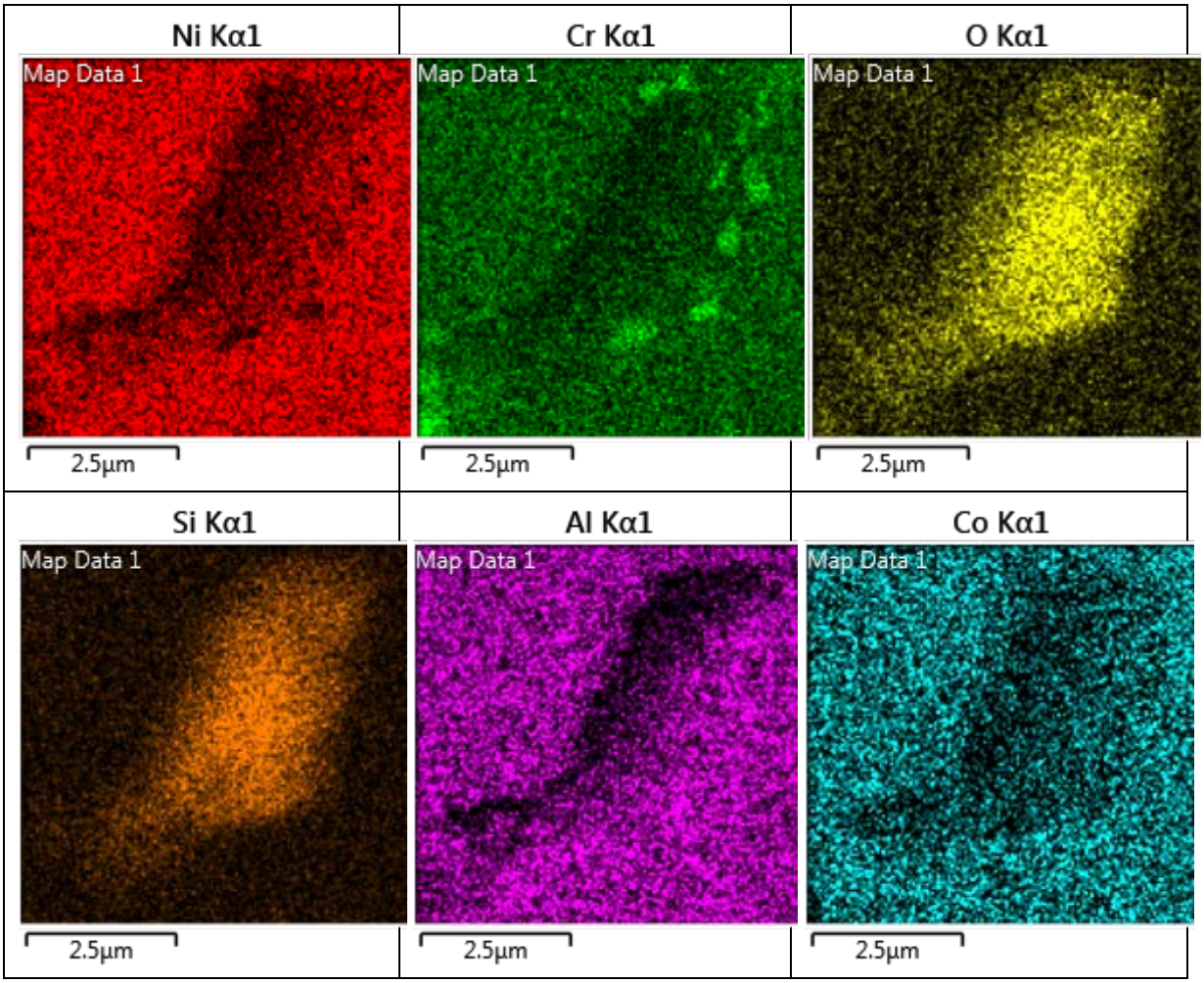

Appendix C4. Resulting map composition for the silica oxide

Sample No.	Bars (#)	Cylinders (#)	HIP-temp (Celsius)	HIP-press (Bar)	HIP-time (hours)	HT-temp (Celsius)	HT-press (Bar)	HT-time (hours)
1, 2	2	2	1210	1000	4	None	None	None
4, 5	2	2	1210	1000	4	850	0	2
6, 7	2	2	1210	1000	4	850	1000	2
8, 9	2	2	1210	2000	4	None	None	None
10, 11	2	2	1210	2000	4	850	0	2
24,25	2	2	1210	2000	4	850	2000	2
16, 17	2	2	1000	1000	4	None	None	None
18, 19	2	2	1000	1000	4	850	0	2
20, 21	2	2	1000	1000	4	850	1000	2
22, 23	2	2	1000	2000	4	None	None	None
14,15	2	2	1000	2000	4	850	0	2
26, 27	2	2	1000	2000	4	850	2000	2

Appendix C 5. Sample number and data for HIP+HT